

# ADER scheme for incompressible Navier-Stokes equations on overset grids with a compact transmission condition

Michel Bergmann<sup>a,b</sup>, Michele Giuliano Carlino<sup>a,b,\*</sup>, Angelo Iollo<sup>a,b</sup>, Haysam Telib<sup>c</sup>

<sup>a</sup> INRIA Bordeaux Sud-Ouest, MEMPHIS team, 200 avenue de la Vielle Tour, 33405 Talence, France

<sup>b</sup> IMB, Institut de Mathématiques de Bordeaux, 351 cours de la Libération, 33405 Talence, France

<sup>c</sup> Optimad srl, via Agostino da Montefeltro 2, 10134 Turin, Italy



## ARTICLE INFO

### Article history:

Received 16 June 2021

Received in revised form 28 February 2022

Accepted 22 June 2022

Available online 8 July 2022

### Keywords:

Chimera mesh

Overset grid

ADER

Finite volume

Incompressible Navier-Stokes

Compact transmission condition

## ABSTRACT

A space-time Finite Volume method is devised to simulate incompressible viscous flows in an evolving domain. Inspired by the ADER method (based on a Finite-Element-prediction/Finite-Volume-correction approach), the Navier-Stokes equations are discretized onto a space-time overset grid which is able to take into account both the shape of a possibly moving object and the evolution of the domain. A compact transmission condition is employed in order to mutually exchange information from one mesh to the other. The resulting method is second order accurate in space and time for both velocity and pressure. The accuracy and efficiency of the method are tested through reference simulations.

© 2022 Elsevier Inc. All rights reserved.

## 1. Introduction

The simulation of flows in complex unsteady geometries such as fluid-structure interaction, freely moving objects or moving boundaries induced by the flow itself requires specific numerical modeling. It is possible to distinguish three main classes of methods for these flow phenomena: the Arbitrary Lagrangian-Eulerian (ALE) methods, interface methods and Chimera meshes approaches. The ALE methods [1,2] are accurate and allow a sophisticated grid displacement and mesh adaptation after a proper reformulation of the governing equations. However, when the grid deformation is affected by an excessive stretch, a computationally expensive remeshing may be necessary. Consequently, further numerical errors deriving from the interpolation of data from the old grid to the new mesh need to be managed. In interface methods, such as Ghost boundary methods [3], immersed boundary methods [4] and penalization methods [5], the physical domain is discretized through a simple mesh, usually structured and Cartesian, not changing in time [6,7]. For this reason, the mesh does not necessarily fit the moving boundary and a special care has to be taken to attain a sufficient degree of accuracy at the physical boundaries. However, because of the simplicity of the mesh and its unique aspect ratio, the presence of thin boundary layers could significantly affect the computational advantages of these methods. Hybrid techniques employing immersed boundary methods with anisotropic mesh adaptations can be employed for circumventing this problem [8].

\* Corresponding author at: IMB, Institut de Mathématiques de Bordeaux, 351 cours de la Libération, 33405 Talence, France.

E-mail addresses: [michel.bergmann@inria.fr](mailto:michel.bergmann@inria.fr) (M. Bergmann), [michele-giuliano.carlino@inria.fr](mailto:michele-giuliano.carlino@inria.fr) (M.G. Carlino), [angelo.iollo@inria.fr](mailto:angelo.iollo@inria.fr) (A. Iollo), [haysam.telib@optimad.it](mailto:haysam.telib@optimad.it) (H. Telib).

Our investigations focus on Chimera grids [9–12]. They consist of multiple overlapping mesh blocks that together define an overset grid [13–15]. The use of Chimera meshes is essentially based on a grid embedding technique for discretizing the possibly evolving computational domain. A major grid (*background grid*) is first built. It is non-conformal with respect to the complex shape of the domain. Then, minor grid(s) (*foreground blocks*) are constructed in order to describe the particular shape of those regions where the obstacles are located. Since the minor blocks overlap the major grid, an overlapping region is defined among all blocks [11]. This mesh generation strategy considerably simplifies the task of mesh adaptation in the case of boundary layers, changing geometry for an unsteady problem and for unsteady multiply connected domains [16–21].

In general, the numerical solution on Chimera grids is obtained by exchanging data through the fringe cells at the overlapping zone. For example, in [22–25], *donor* cells of a block in proximity of the overlapping zone provide the information to *receptor* cells of another block by polynomial interpolation. In [26] a different strategy is pursued. A coarse grid is automatically generated and a connection of interpolation information at the overlapping zone is presented through a multigrid approach. Yet another way of making the different blocks communicate is to use some kind Domain Decomposition (DD) methods (e.g., Schwartz, Dirichlet/Neumann or Dirichlet/Robin methods). In particular, each mesh block is considered as a decomposition of the domain and the overlapping zones are the interfaces for coupling the different blocks. Accordingly to these approaches, iterative discrete methods are employed. For this two-way communication, the reader is referred to [27] for further details.

Different approaches connect the background and the foreground meshes, such as the DRAGON grids [28] for which the overlapping zone is replaced by a unstructured grid during a further stage by preserving the body-fitting advantages of the Chimera meshes. In essence, a DRAGON grid consists in creating a unique block mesh from a Chimera configuration. However, the computational costs to generate a DRAGON grid for an evolving domain can be significant since at every time instance a new DRAGON mesh needs to be built.

In this paper, we propose a space-time Finite Volume (FV) scheme on Chimera grids. Our objective is to combine some aspects of an ALE approach, notably its flexibility with respect to grid displacement and deformation, to the multi-block discretization strategy of overset grids. In particular, special care is devoted to grid overlapping zones in order to devise a compact and accurate discretization stencil to exchange information between different mesh patches. In this regard, a compact transmission condition is sought to limit communications between the grids as in [29]. This means that the stencil constructed for the discretization at a specific cell is based only on the first layer of its surrounding cells. A second order transmission condition is then devised by properly defining a stencil that belong to *both* the back- and foreground meshes, over which the solution is interpolated in space and time by a suitable polynomial. This hybrid stencil allows a smooth discretization transition from one block to another. In particular, first a mesh-free discontinuous FEM-solution is recovered and then a FVM-correction is performed in any cell by using information provided by neighboring cells. Thus, for fringe cells, the solution is obtained by combining values from different grids.

Overall, for the numerical solution of the incompressible Navier-Stokes equations we follow a classical prediction-projection-correction method [30,31] with a second-order accuracy in space and time. The Arbitrary high order DERivatives (ADER) method provides an ideal setting for the resolution of the nonlinear unsteady convection-diffusion equation with a moving grid. In [32–35], the authors present a method to recover an accurate solution for hyperbolic differential problems with an arbitrary order of accuracy on a single mesh block. The numerical scheme treats the temporal variable indistinctly with respect to the spatial variables by defining the solution on a space-time slab. This discretization approach, therefore, allows us to re-consider the problem of Chimera grids transmission conditions. Instead of time-dependent spatial transmission conditions between relatively moving grid blocks, we define interpolation polynomials on arbitrarily intersecting space-time cells at the block boundaries. In the ADER scheme a local space-time weak solution of the problem from the generic time  $t$  to  $t + \Delta t$  is computed in every single space-time cell. This solution is defined as the *predictor*. The prediction step is local and hence embarrassingly parallel, because the solution is calculated independently of the information of the neighboring cells. Then, in the subsequent stage of *correction*, the computation of a space-time numerical flux between neighboring cells provides the appropriate stabilization of the integration scheme. We extend this method for the incompressible Navier-Stokes equations on overset grids, in the spirit of our previous work [36].

For the resolution of the Poisson equation in the projection step, we propose a hybrid FV method. On internal cells, a classical reconstruction of the gradient through the diamond formula [37,38] is employed. On fringe cells, namely the ones on the boundary of the overlapping zone, inspired by [39], the reconstruction of the gradient is performed by interpolating the data through an appropriate local minimization taking into account the geometry of the stencil. A characteristic property of interpolation at the interface between meshes is conservation. Nonconservative schemes (the most commonly used) are based on the local study of the particular overlapping configuration of cells used to define the interpolation itself [20]. The conservative interpolations, on the other hand, include patched interfaces [40,41] or arbitrary overlapping regions [42,43]. In general, these schemes are less attractive because, although they are relatively easy to implement in two dimensions, their application in three dimensions becomes cumbersome. Moreover, even if global conservation of fluxes between overlapping boundaries or at the boundary of holes is guaranteed, local conservation of fluxes cannot generally be obtained. In our scheme for the Poisson equation, special care is devoted to the definition of a fully conservative scheme in the limit of a no-shift overlapping configuration, namely when the background and foreground meshes coincide in the overlapping region.

Among previous and related approaches, the first schemes using overset grids for the incompressible Navier-Stokes equations are those by Volkov [9] and Starius [14]. Successively, we mention for example [44–46,10,41,20] for the numerical

solution a wide range of PDEs. It is possible to group them into two main categories: Fractional Step methods (FSM) and Domain Decomposition (DD) approaches. Among the works using a FSM, we cite a recent paper<sup>1</sup> by Meng et al. [47] where the authors achieve a fourth order accuracy. Concerning the DD approaches, one of the last works is by Mittal, Dutta and Fischer [48], in which a Schwarz-spectral approach is used by decomposing the domain with respect to the different blocks of the overset grid. All these works have in common the fact that fringe cells, namely the cells at the boundary of the overlapping regions, exchange the information by a proper interpolation. In general, a special effort is devoted to the definition of a quick and efficient interpolation ensuring the required order of accuracy for the final solution [47,48]. In particular, one of the most recent works by Sharma et al. [49] defines the following differentiation of the nodes of an overset grid:

- **Field points:** mesh nodes at which the governing equations are solved;
- **Fringe points:** mesh nodes at which the information is transferred between overlapping meshes;
- **Hole points:** mesh nodes at which the solution does not exist.

In this work we do not resort to this classical nodes clustering. Since we employ an ADER approach and spend part of the global computational costs for finding a compact stencil at the overlapping interfaces, we never need to exchange information by interpolation. In particular, as it will be clear along the paper, the prediction step of ADER defines a free-mesh approach for which all nodes are undistinguished with respect to the classical clustering; successively, in the subsequent correction step, due to the definition of a hybrid stencil composed of nodes belonging to different meshes, the finite volume approach allows to automatically exchange the information of the previous step. The only interpolation is mandatory when a hole cell turns into an active cell due to the movement of the foreground mesh.

For the projection step (Poisson step), fringe cells are no longer exploited as donors or receptors of information. As a matter of fact, a proper discretization of the gradient operator is proposed at the interfaces using all the information of the compact hybrid stencil. Consequently, the relations described by the stiffness matrix resulting from the discretization of the Laplace operator automatically manages the exchange of information without going through a subsequent interpolation step.

The current state of the art considers chimera grids as discretization of the space. Due to the ADER method, the proposed overset grids discretize the space-time continuum and, consequently, define space-time chimera meshes. This is an advantage that allows to evolve the domain as well as the overset grid (with a possible dependency on the solution itself) and, at the same time, to compute the solution over this evolving computational structure.

## 2. The overset grid

An overset grid or Chimera mesh is a set of mesh blocks covering the computational domain. Each block may overlap other block(s) in some particular sub-region(s) said *overlapping zone(s)*. Once the multiple mesh patches are generated, they are collated in order to have an appropriate topology [11]. Consequently, a hole of inactive cells is defined in the background partition. In the sequel, the method is explained by considering a two block overset grid (i.e., the background and the foreground meshes). Fig. 1 shows an overset grid composed by one background mesh (in black) surrounding one foreground mesh (in blue). In many situations, the foreground mesh can move and deform. The overlapping zone is necessary for the communication and data transfer from one mesh to the other.

By considering the notation introduced in Fig. 1, surface  $\partial\Omega_{ig}/\Gamma_S$  is the outer boundary of the subdomain discretized by the foreground partition. The hole-cutting takes place for all those cells whose centers of mass lie within the  $n$ -th layer of foreground cells starting from the foreground outer boundary. In the presented numerical results,  $n = 5$ .

The computational cell of any block mesh is quadrilateral in this work.

### 2.1. Automatic definition of the stencil and transmission condition

Let  $\mathcal{T}_k = \{\Omega_i^k\}_{i=1}^{N_k}$  be the partition composed of  $N_k$  cells referring to the  $k$ -th block mesh. In order to simplify the notation, in the following we will omit the superscript  $k$  to the cell  $\Omega_i^k$  by writing  $\Omega_i$ . Let  $\mathcal{S}_i$  the stencil centered over the cell  $\Omega_i$ . Thus, stencil  $\mathcal{S}_i$  is the set collecting the indexes of neighboring cells to  $\Omega_i$ . By abuse of language, sometimes we will refer to the physical set  $\Omega_i \cup \bigcup_{j \in \mathcal{S}_i} \Omega_j$  as the stencil.

It is possible to distinguish two classes of cells with respect to their proximity to the overlapping interface. The definition of the stencil depends on the class it belongs to.

If cell  $\Omega_i$  is not at the boundary of the overlapping zone (Fig. 2a), the stencil  $\mathcal{S}_i$  is composed of all the cells  $\Omega_j$  sharing at least one vertex with  $\Omega_i$ . Thus, if  $\Omega_i$  belongs to the partition  $\mathcal{T}_1$ , all cells  $\Omega_j$ , with  $j \in \mathcal{S}_i$ , also belong to  $\mathcal{T}_1$ .

If the cell  $\Omega_i$  of partition  $\mathcal{T}_k$  is at the boundary of the interface, it is no longer possible to use the criterion of the cells sharing at least a vertex. In fact, there will be at least one edge  $e_{il}$  not shared by any other cell of the same partition (see left edges of cell  $\Omega_{16}$  in Fig. 2b). For these cells, we systematically identify other cells of partition  $\mathcal{T}_j$  ( $j \neq k$ ) belonging to

<sup>1</sup> This paper is listed in the **Overture** website <https://www.overtureframework.org/publications.html>. We refer the reader to this website for an exhaustive bibliography related to the overset grids.

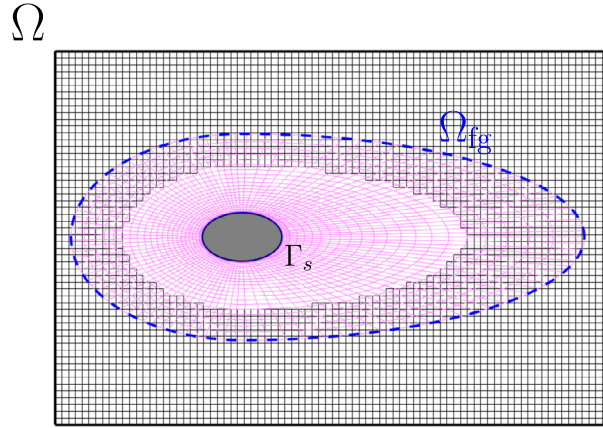
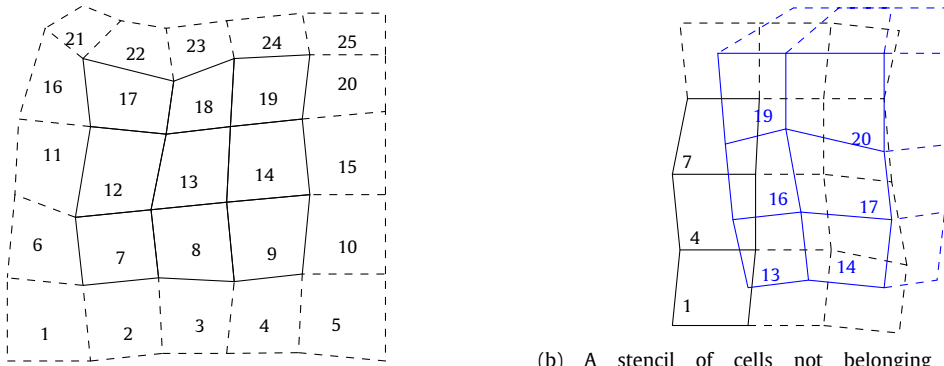


**Fig. 1.** Sketch of the mesh configuration. The computational (i.e. fluid) domain contains the solid body whose boundary is  $\Gamma_s$ . The foreground mesh (in blue) defines the foreground subdomain  $\Omega_{fg}$  whose boundary is the union of an external (dashed line) and internal (continuous line) boundary. Consequently, the internal foreground boundary coincides with the solid body boundary. To appreciate the figures at best, the reader is referred to the color electronic version of this paper.



(a) A stencil of cells in the same partition. Continuous line for the stencil  $\mathcal{S}_{13} = \{7, 8, 9, 12, 14, 17, 18, 19\}$ .

(b) A stencil of cells not belonging to the same partition. Continuous line for the stencil  $\mathcal{S}_{16} = \{1, 4, 7, 13, 14, 17, 19, 20\}$ .

**Fig. 2.** Two possible stencils: on the right the stencil is in the same partition; on the left the stencil is composed of cells not belonging to the same partition.

the stencil. Let the extremes of the edge be indicated as  $\mathbf{v}_1$  and  $\mathbf{v}_2$  and its middle point with  $\mathbf{v}_3$ , respectively. Point  $\mathbf{c}_*$  is the center of mass of generic cell  $\Omega_*$ . For our numerical tests, Algorithm 1 is adopted through the two steps:

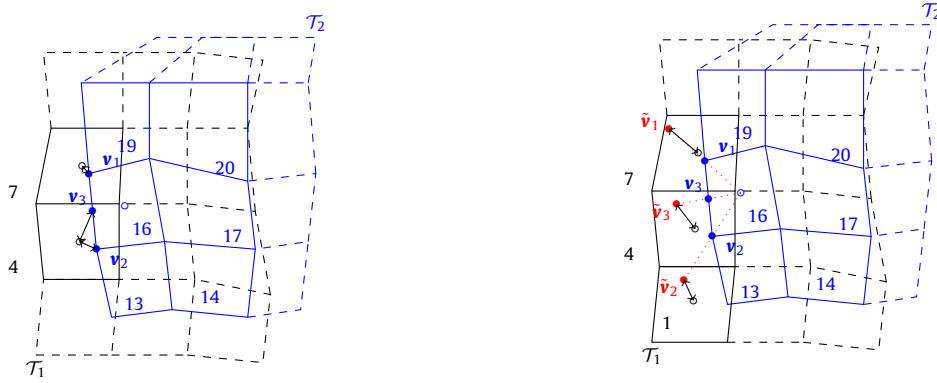
1. look for the nodes of cells of the other partition  $\mathcal{T}_j$  minimizing the Euclidean distance with respect to points  $\mathbf{v}_\mu$ ,  $\mu = 1, 2, 3$ , (line 5, see Fig. 3a);
2. compute the symmetric points  $\tilde{\mathbf{v}}_\mu$  of center  $\mathbf{c}_i^k$  with respect to points  $\mathbf{v}_\mu$  for  $\mu = 1, 2, 3$  (line 6), then look for the cells of partition  $\mathcal{T}_j$  whose centers minimize the Euclidean distance with the three symmetric points (line 7, see Fig. 3b).

For the edges shared by other cells in the same partition, the cells of the stencil will be those ones sharing at least one vertex (as cells of indexes 13, 14, 17, 19 and 20 in Fig. 2b).

The routine presented in this section will be run whenever the foreground mesh configuration as well as the hole change.

Algorithm 1 could not define a compact stencil in the case of widely different mesh spacing between the two blocks. In that case, more than three points for lines 5 and 7 could be considered. Moreover, a weighted symmetry (possibly led by the difference between the mesh spacing) could be performed at line 6.

Concerning the hole-cutting process, in our code the surface defined by the foreground cells distant five layers of cells from the boundary is identified; successively all cells in the background whose centers fall inside this surface are flagged as inactive points. Fringe cells (on the different blocks) are identified as the ones on the cut, in background, and at the boundary of the foreground; finally, over them the hybrid stencil is built via Algorithm 1. For a deep literature review on the assembling process regarding the mesh blocks definition and the hole-cutting, we address the reader to [50] and its bibliography.



(a) First step: by identifying the vertexes  $\mathbf{v}_1$  and  $\mathbf{v}_2$  and the middle point  $\mathbf{v}_3$  of the edge on the boundary cell  $\Omega_{16}$  (blue full dots), look for the nodes of cells in the partition  $\mathcal{T}_1$  (black empty dots) minimizing the Euclidean distance with respect to those points.

(b) Second step: by identifying the symmetric points  $\tilde{\mathbf{v}}_\mu$ ,  $\mu = 1, 2, 3$ , (red full dots) of the node of the cell  $\Omega_{16}$  (blue empty dot) with respect to the vertexes and the middle point of the non-shared edge, look for the nodes of cells in the partition  $\mathcal{T}_1$  minimizing the Euclidean distance to those points.

**Fig. 3.** The two steps for the research of cells in the partition  $\mathcal{T}_1$  for the cell  $\Omega_{16} \in \mathcal{T}_2$ . To appreciate the figures at best, the reader is referred to the color electronic version of this paper.

**Algorithm 1** Compute stencil for cells at the boundary of the overlapping zone.

**Require:**  $\Omega_i^k, e_{ij}^k, \mathcal{T}_j, S_i^k$ ;  
 1: Initialize  $\mathbf{v}_1$  and  $\mathbf{v}_2$  as the two vertexes of edge  $e_{ij}^k$ ;  
 2:  $\mathbf{v}_3 \leftarrow (\mathbf{v}_1 + \mathbf{v}_2)/2$ ;  
 3:  $\mathcal{Z}_j \leftarrow \emptyset$ ;  
 4: **for**  $\mu = 1, 2, 3$  **do**  
 5:  $\mathcal{Z}_j \leftarrow \mathcal{Z}_j \cup \{n = 1, \dots, N_j : \|\mathbf{v}_\mu - \mathbf{c}_n^j\| \leq \|\mathbf{v}_\mu - \mathbf{c}_m^j\| \quad \forall m = 1, \dots, N_j\}$ ;  
 6:  $\tilde{\mathbf{v}} \leftarrow 2\mathbf{v}_\mu - \mathbf{c}_i^k$ ;  
 7:  $\mathcal{Z}_j \leftarrow \mathcal{Z}_j \cup \{n = 1, \dots, N_j : \|\tilde{\mathbf{v}} - \mathbf{c}_n^j\| \leq \|\tilde{\mathbf{v}} - \mathbf{c}_m^j\| \quad \forall m = 1, \dots, N_j\}$ ;  
 8:  $S_i^k \leftarrow S_i^k \cup \mathcal{Z}_j$ ;  
 9: **return**  $S_i^k$

▷  $j \neq k$ , i.e.  $\mathcal{T}_j$  is the other partition with respect to  $\mathcal{T}_k$   
 ▷ Middle point of edge  $e_{ij}^k$   
 ▷ Temporary set of indexes of partition  $\mathcal{T}_j$   
 ▷ Symmetric point of cell-center  $\mathbf{c}_i^k$  of  $\Omega_i^k$  with respect to  $\mathbf{v}_\mu$

**3. The governing equations**

Let  $\Omega(t) \subset \mathbb{R}^2$  be the computational domain, eventually evolving in time  $t \in [0, T]$ , with  $T$  positive real. We aim in studying the two-dimensional incompressible flow in the space-time domain  $\Omega(t) \times (0, T)$  governed by the system

$$\rho \left( \frac{\partial \mathbf{u}}{\partial t} + (\mathbf{u} \cdot \nabla) \mathbf{u} \right) = -\nabla p + \mu \Delta \mathbf{u} \quad \text{in } \Omega(t) \times (0, T), \tag{1a}$$

$$\nabla \cdot \mathbf{u} = 0 \quad \text{in } \Omega(t) \times (0, T), \tag{1b}$$

$$\mathbf{u}(\mathbf{x}, 0) = \mathbf{u}_0(\mathbf{x}) \quad \text{in } \Omega(0) \times \{0\}, \tag{1c}$$

and completed with boundary conditions over  $\partial\Omega(t) \times (0, T)$ . In system (1), the unknowns are the velocity  $\mathbf{u}$  and the pressure  $p$  of the fluid of density  $\rho$  and dynamic viscosity  $\mu$ . The initial condition is given by (1c) through the initial velocity  $\mathbf{u}_0$ . Sometimes, it is more convenient to study the nondimensionalized system of (1); in this case, through the incompressibility condition (1b), equations (1a) become

$$\frac{\partial \mathbf{u}}{\partial t} + \nabla \cdot (\mathbf{u} \mathbf{u}^T) = -\nabla p + \frac{1}{\text{Re}} \Delta \mathbf{u} \quad \text{in } \Omega(t) \times (0, T), \tag{2}$$

where  $\text{Re} = \rho u_\infty L / \mu$  is the Reynolds number, with  $u_\infty$  the characteristic velocity of the fluid and  $L$  the characteristic length of either the physical domain or the obstacle, if it is present.

The domain  $\Omega(t)$  is discretized with an overset mesh whose background and foreground partitions are  $\mathcal{T}_{bg}$  and  $\mathcal{T}_{fg}$ , respectively. For the sake of simplicity we consider only one foreground mesh even though it is possible to extend the method by employing several foreground meshes. The cells of the foreground partition define a subset  $\Omega_{fg}$  of the physical domain. The foreground mesh of coordinates  $\mathbf{X}$  is allowed to move and deform accordingly to the motion equation

$$\frac{d\mathbf{X}}{dt} = \mathbf{V} \quad \text{in } (0, T), \tag{3}$$

which is a Cauchy problem of initial condition  $\mathbf{X}|_{t=0} = \mathbf{X}_0(\mathbf{x})$ . In problem (3) the force term is the mesh velocity  $\mathbf{V}(\mathbf{x}, t; \mathbf{u}, p)$ , eventually dependent on the fluid velocity and pressure (in that case systems (1) and (3) are coupled). The motion equation (3) can be imposed regardless of the physics described by system (1). However, when studying fluid-structure interaction phenomena, the foreground mesh is employed in order to easily take into account the generic shape of the solid body. Consequently, the computational domain  $\Omega(t)$  defines the fluid domain and part of the boundary of the foreground subdomain  $\Omega_{\text{fg}}$  discretizes the boundary  $\Gamma_s$  of the solid, i.e.,  $\Gamma_s \subset \partial\Omega_{\text{fg}}$  (see Fig. 1). Along the boundary  $\Gamma_s$  the interaction between the fluid and the solid takes place and it mathematically reads

$$\mathbf{u} = \mathbf{u}_B \quad \text{on } \Gamma_s(t) \times (0, T), \tag{4}$$

where  $\mathbf{u}_B$  is the velocity of the solid body. Thus, the mesh velocity  $\mathbf{V}$  has to coincide with the velocity  $\mathbf{u}_B$  of the body on the boundary  $\Gamma_s$  of the solid:

$$\mathbf{V}|_{\Gamma_s} \equiv \mathbf{u}_B. \tag{5}$$

Consequently, the dynamics of motion and deformation of the foreground mesh in (3) is led by condition (5).

#### 4. The numerical method

The Navier-Stokes equations (1) are discretized using a Finite Volume (FV) scheme with the collocated cell-centered variables  $(\mathbf{u}, p)$ . Let the whole time interval  $(0, T)$  be subdivided into  $N$  sub-intervals  $(t^n, t^{n+1})$ ,  $n = 1, \dots, N - 1$ , of length  $\Delta t$ . For a given variable  $\phi(\mathbf{x}, t)$ , we indicate its evaluation at discrete time  $t^n$  with  $\phi^n$ . A fractional step method is used to evaluate the solution in time. In order to improve the pressure smoothness and avoid odd-even oscillation phenomena, the face-centered velocity

$$\mathbf{U} = (\mathbf{u})_{\text{fc}} \tag{6}$$

is introduced as presented by Mittal et al. [51]. The symbol  $(\cdot)_{\text{fc}}$  is a discrete operator computing the face-centered value of the cell-centered input and it will be explained at the end of this section.

Based on the predictor-projection-correction non incremental Chorin-Temam scheme [30,31], the first step (predictor step) evaluates an intermediate velocity  $\mathbf{u}^*$  obtained by the resolution of an unsteady convection-diffusion equation

$$\begin{cases} \frac{\partial \mathbf{u}^*}{\partial t} + \nabla \cdot (\mathbf{u}^* \mathbf{U}^n)^T - \frac{1}{\text{Re}} \Delta \mathbf{u}^* = \mathbf{0} & \text{in } \Omega(t) \times (t^n, t^{n+1}) \\ \mathbf{u}^* = \mathbf{u}^n & \text{in } \Omega^n \times \{t^n\} \end{cases}, \tag{7}$$

which will be numerically solved as explained in the next subsection.

The intermediate velocity  $\mathbf{u}^*$  solving problem (7) is not divergence free. Thus the predicted field  $\mathbf{u}^*$  is projected onto a divergence free space through the pressure. As a matter of fact, by computing the divergence of equation

$$\frac{\mathbf{u}^{n+1} - \mathbf{u}^*}{\Delta t} = -\nabla p^{n+1} \quad \text{in } \Omega(t) \times (t^n, t^{n+1}) \tag{8}$$

and applying the divergence condition (1b) on the velocity fluid  $\mathbf{u}^{n+1}$ , we obtain the Poisson equation for the pressure

$$\Delta \psi^{n+1} = \nabla \cdot \mathbf{u}^* \quad \text{in } \Omega^{n+1}, \tag{9}$$

with  $\psi = \Delta t p$ , by defining the projection step. Problem (9) refers to the cell-centered velocity field and pressure. Thus, by employing the face-centered intermediate velocity  $\mathbf{U}^* = (\mathbf{u}^*)_{\text{fc}}$ , problem (9) turns into

$$\Delta \psi^{n+1} = \nabla \cdot \mathbf{U}^* \quad \text{in } \Omega^{n+1}, \tag{10}$$

which is numerically solved as explained in Section 4.2.

The velocity fields  $\mathbf{u}^{n+1}$  and  $\mathbf{U}^{n+1}$  at the cell-centers and face-centers, respectively, are finally corrected through equation (8) as

$$\mathbf{u}^{n+1} = \mathbf{u}^* - \nabla \psi^{n+1}, \tag{11a}$$

$$\mathbf{U}^{n+1} = \mathbf{U}^* - (\nabla \psi^{n+1})_{\text{fc}}, \tag{11b}$$

which conclude the numerical routine within the time sub-interval from  $t^n$  to  $t^{n+1}$ .

#### 4.1. The predictor solution

In this subsection the numerical scheme for the predictor equation (7) solved by the intermediate velocity  $\mathbf{u}^*$  is presented. The method consists in a FV predictor-corrector scheme stabilized with a Local Lax-Friederichs approach. It was originally presented in our previous work [36] for a generic advection-diffusion (eventually nonlinear) problem where the computational domain is discretized by employing overset grids. It is inspired by the ADER (Arbitrary high-order DERivatives) method [32–35] and was reformulated for both the presence of the diffusion and the management of the dynamics for the Chimera mesh.

##### 4.1.1. Local space-time Galerkin predictor and foreground mesh motion

The first step of the method for the unsteady convective-diffusive equation (7) consists in the research of a weak solution in any cell of the mesh. Let  $C_i^n = \Omega_i(t) \times (t^n, t^{n+1})$  be the physical space-time cell whose lower and upper bases represent the evolution of the  $i$ -th cell  $\Omega_i(t)$  from time  $t^n$  to  $t^{n+1}$ . Problem (7) is rewritten with respect to a space-time reference system identified by the independent variables  $\xi \equiv (\xi, \eta, \tau)$  in the unit cube  $\hat{C} = (0, 1)^3$ . As originally proposed in [52], it is discretized through a nodal formulation of space-time nodes given by a tensor product of three Gauss-Legendre quadrature points, namely  $\{1/2, (5 \pm \sqrt{15})/10\}$ , along space and time directions. This choice defines an  $L^2(\hat{C})$ -orthogonal Lagrange basis used for the approximation of the Galerkin solution. Consequently, over a space-time cell there are 27 Gauss-Legendre nodes  $\hat{\xi}_m$  and 27 Lagrange polynomials  $\theta_l: \hat{C} \rightarrow \mathbb{R}$  such that

$$\theta_l(\hat{\xi}_m) = \delta_{lm} \quad \text{and} \quad \int_{\hat{C}} \theta_l \theta_m \, d\xi = \delta_{lm}, \quad l, m = 1, \dots, 27,$$

where  $\delta_{lm}$  is the Kronecher symbol.

The component-wise problem to be solved is: find  $q_k: C_i^n \rightarrow \mathbb{R}, k = 1, 2$ , such that

$$\begin{cases} \partial_t q_k + \nabla \cdot \mathbf{F}(q_k, \nabla q_k) = 0 & \text{in } C_i^n \\ q_k = \Pi_i u_k^n & \text{on } \Omega_i^n \end{cases}, \quad (12)$$

where  $\mathbf{F}(q_k, \nabla q_k) = \mathbf{q}q_k - \nabla q_k/\text{Re}$  is the convective-diffusive term. Problem (12) is problem (7) restricted to the physical space time-cell  $C_i^n$  and redefined as a boundary value problem. Let  $E_i^n$  be the union of all cells belonging to the stencil  $S_i^n$  centered on cell  $\Omega_i^n$  identified by the cell-center  $\mathbf{x}_i^n$  (i.e.,  $E_i^n = \Omega_i^n \cup \bigcup_{j \in S_i^n} \Omega_j^n$ ). Function  $\Pi_i \phi$  is the polynomial interpolation of a given function  $\phi \in C^2(E_i^n)$ , whose knowledge is only available to the cell-centers, by employing the quadratic basis of the polynomial space function

$$\mathcal{P}_2(E_i^n) = \text{span} \left\{ 1, x - x_i^n, y - y_i^n, (x - x_i^n)(y - y_i^n), \frac{1}{2}(x - x_i^n)^2, \frac{1}{2}(y - y_i^n)^2 \right\}.$$

In order to find the polynomial coefficients related to this basis, the constrained  $\Pi_i u_k^n(\mathbf{x}_j) \equiv u_k^n(\mathbf{x}_j)$  for any  $j \in S_i^n$ . The way the stencils are constructed, the constraints are always more than the components of the basis  $\mathcal{P}_2(E_i^n)$ . Thus, the polynomial coefficients are found in the mean-square sense.

We remark that at this stage the face-centered velocity field  $\mathbf{U}$  is not required as originally indicated in problem (7).

In order to refer problem (12) to the reference domain  $\hat{C}$ , we use a map  $\mathcal{M}_i: \hat{C} \rightarrow C_i^n$

$$\mathcal{M}_i: \begin{cases} x = x(\xi, \eta, \tau) \\ y = y(\xi, \eta, \tau) \\ t = t^n + \Delta t \tau \end{cases}, \quad (13)$$

such that any space-time point  $\mathbf{x} \equiv (x, y, t)$  in the physical space-time cell  $C_i^n$  is a function  $\mathbf{x} = \mathbf{x}(\xi)$ , with  $\xi \in \hat{C}$  (see Fig. 4). Time  $t$  is considered as linear function of  $\tau$  of slope  $\Delta t$ . From map (13), the Jacobian matrix  $J$  reads

$$J = \frac{d\mathbf{x}}{d\xi} = \begin{bmatrix} x_\xi & x_\eta & x_\tau \\ y_\xi & y_\eta & y_\tau \\ 0 & 0 & \Delta t \end{bmatrix}, \quad (14)$$

whose inverse is

$$J^{-1} = \frac{d\xi}{d\mathbf{x}} = \begin{bmatrix} \xi_x & \xi_y & \xi_t \\ \eta_x & \eta_y & \eta_t \\ 0 & 0 & 1/\Delta t \end{bmatrix}. \quad (15)$$

Moreover, let  $J_s^{-1}$  be the restriction to the spatial coordinates of the inverse of the Jacobian matrix (15):

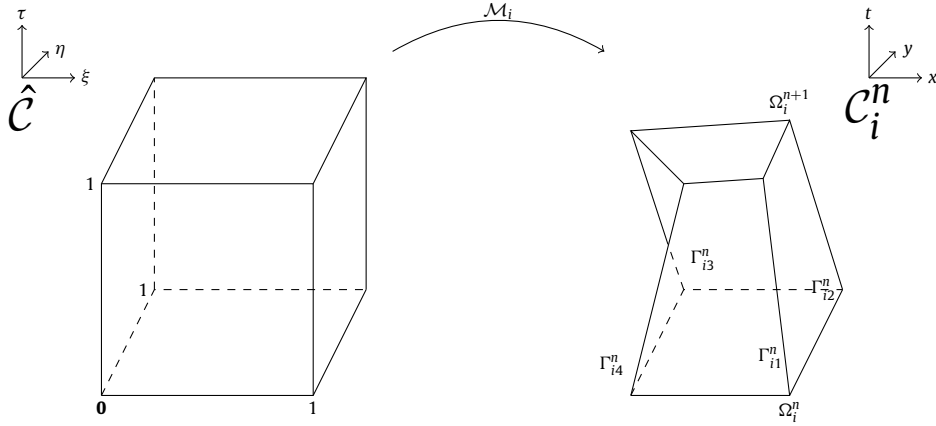


**Fig. 4.** Sketch of the map  $\mathcal{M}_i$  from the reference space-time cell  $\hat{C}$  to the physical space-time cell  $C_i^n$ . The boundary  $\partial C_i^n$  of the physical space-time cell is defined by the spatial cells  $\Omega_i^n$  (lower base) and  $\Omega_i^{n+1}$  (upper base) and by the space-time boundaries  $\Gamma_{ij}^n$ ,  $j = 1, \dots, 4$ , linking any edge of  $\Omega_i^n$  to any edge of  $\Omega_i^{n+1}$ .

$$J_s^{-1} = \begin{bmatrix} \xi_x & \xi_y \\ \eta_x & \eta_y \end{bmatrix}. \tag{16}$$

Through (16), the problem in the reference domain reads<sup>2</sup>

$$\partial_\tau q_k + \Delta t \mathcal{F}^\flat(\hat{\nabla} q_k) + \Delta t J_s^{-T} \hat{\nabla} \cdot \mathcal{F}^\sharp(q_k, \hat{\nabla} q_k) = 0 \quad \text{in } \hat{C}, \tag{17}$$

with

$$\mathcal{F}^\flat(\hat{\nabla} q_k) = \begin{bmatrix} \xi_t \\ \eta_t \end{bmatrix} \cdot \hat{\nabla} q_k; \quad \mathcal{F}^\sharp(q_k, \hat{\nabla} q_k) = \mathbf{F}(q_k, J_s^{-T} \hat{\nabla} q_k) = \begin{bmatrix} \mathcal{F}_{\xi\xi}^\sharp \\ \mathcal{F}_{\xi\eta}^\sharp \\ \mathcal{F}_{\eta\xi}^\sharp \\ \mathcal{F}_{\eta\eta}^\sharp \end{bmatrix}; \quad \hat{\nabla} = \begin{bmatrix} \partial_\xi \\ \partial_\eta \end{bmatrix}.$$

The hat differential operators refer to the reference space variables  $\xi$  and  $\eta$  in the reference space-time cell  $\hat{C}$ . By abuse of notation and for the sake of simplicity, the solutions  $q_k$  involved in both equations (12) and (17) are defined with the same symbol even though they take inputs in the physical space-time cell  $C_i^n$  and in the reference space-time cell  $\hat{C}$ , respectively. In order to weaken the problem (17), we introduce the following functional space

$$\Theta = \left\{ v \in L^2(\hat{C}) : (0, 1)^2 \ni (\xi, \eta) \mapsto v(\xi, \eta, \tau) \in H^1((0, 1)) \right\}$$

as subspace of energy-finite functional space  $L^2(\hat{C})$  of functions that associate a Sobolev  $H^1((0, 1))$ -integrable function for any fixed reference spatial variables  $(\xi, \tau)$ . Moreover, we use the following notation for any function  $f$  and  $g$  in  $\Theta$ :

$$\langle f, g \rangle = \int_{\hat{C}} f g \, d\xi; \quad [f, g]_\tau = \int_0^1 \int_0^1 f(\xi, \eta, \tau) g(\xi, \eta, \tau) \, d\xi d\eta.$$

Finally, for our purposes, it is identified  $\Theta$  as a test functional space and a trial functional space  $Q_k$  is defined as

$$Q_k = \left\{ v \in \Theta : v(\xi, \eta, 0) = \Pi_i u_k^n(x(\xi, \eta, 0), y(\xi, \eta, 0), t^n) \wedge J^{-1} \begin{bmatrix} \hat{\nabla} v \\ \partial_\tau v \end{bmatrix} \in L^2(\hat{C}; \mathbb{R}^3) \right\}. \tag{18}$$

By multiplying left and right side of (17) by a generic test function  $\theta$  in  $\Theta$  and by integrating over the reference space-time cell  $\hat{C}$ , the weak problem reads: find  $q_k \in Q_k$  such that

$$[q_k, q_k]_1 - \langle \partial_\tau \theta, q_k \rangle + \Delta t \langle \theta, \mathcal{F}^\flat(\hat{\nabla} q_k) \rangle + \Delta t \langle \theta, J_s^{-T} \hat{\nabla} \cdot \mathcal{F}^\sharp(q_k, \hat{\nabla} q_k) \rangle = [\theta, \Pi_i u_k^n]_0 \quad \forall \theta \in \Theta. \tag{19}$$

<sup>2</sup> Because of the transformation, it holds

$$\partial_t q_k = \frac{\partial_\tau q_k}{\Delta t} + \mathcal{F}^\flat(\hat{\nabla} q_k); \quad \text{and} \quad \nabla = J_s^{-T} \hat{\nabla}.$$

For the above equation, for the solution  $q_k$  and the reference convective-diffusive terms  $\mathcal{F}^\flat$  and  $\mathcal{F}^\sharp$  a Lagrangian polynomial expansion is performed by employing the already presented Lagrange basis, thus, by adopting the Einstein notation,  $q_k = \theta_l \hat{q}_{k,l}$  and  $\mathcal{F}^\star = \theta_l \mathcal{F}_l^\star$ , with  $\star = \flat, \sharp$  and  $l = 1, \dots, 27$ , where  $\hat{q}_{k,l} = q_k(\hat{\xi}_l)$  and  $\mathcal{F}_l^\star = \mathcal{F}^\star|_{\hat{\xi}_l}$ . Considering as test function the  $m$ -th Lagrangian polynomial  $\theta_m$  and by using the Lagrangian expansion, we rewrite the equation (19) as

$$([\theta_m, \theta_l]_1 - \langle \partial_\tau \theta_m, \theta_l \rangle) \hat{q}_{k,l} + \Delta t \langle \theta_m, \theta_l \rangle \hat{\mathcal{F}}_l^\flat + \Delta t \langle \theta_m, (\xi_x \partial_\xi + \eta_x \partial_\eta) \theta_l \rangle \mathcal{F}_{\xi,l}^\sharp + \Delta t \langle \theta_m, (\xi_y \partial_\xi + \eta_y \partial_\eta) \theta_l \rangle \mathcal{F}_{\eta,l}^\sharp = [\theta_m, \Pi_i u_k^n]_0, \tag{20}$$

for any  $m = 1, \dots, 27$ . In the left hand side of (20), the arising matrices have a sparse pattern due to the  $L^2$ -orthogonality of the Lagrangian basis (e.g. the mass matrix by  $\langle \theta_m, \theta_l \rangle$  is diagonal). Matrices involving the derivatives of the map  $\mathcal{M}_i$ , i.e.  $\langle \theta_m, (\xi_x \partial_\xi + \eta_x \partial_\eta) \theta_l \rangle$  and  $\langle \theta_m, (\xi_y \partial_\xi + \eta_y \partial_\eta) \theta_l \rangle$ , cannot be explicitly computed before finding the map itself. On the contrary, the components which do not involve the map, namely  $([\theta_m, \theta_l]_1 - \langle \partial_\tau \theta_m, \theta_l \rangle)$  and  $\langle \theta_m, \theta_l \rangle$ , can be pre-computed once for all before solving problem (20). The above equation (20) is nonlinear due to the convective-diffusive terms  $\mathcal{F}^\flat$  and  $\mathcal{F}^\sharp$  which depend on the solution  $q_k$ . For this reason a fixed point problem is solved: let  $r$  be the index of the fixed point iteration, therefore we solve  $q_k^{r+1}$

$$([\theta_m, \theta_l]_1 - \langle \partial_\tau \theta_m, \theta_l \rangle) \hat{q}_{k,l}^{r+1} + \Delta t \langle \theta_m, \theta_l \rangle \hat{\mathcal{F}}_l^{\flat,r} + \Delta t \langle \theta_m, (\xi_x \partial_\xi + \eta_x \partial_\eta) \theta_l \rangle \mathcal{F}_{\xi,l}^{\sharp,r} + \Delta t \langle \theta_m, (\xi_y \partial_\xi + \eta_y \partial_\eta) \theta_l \rangle \mathcal{F}_{\eta,l}^{\sharp,r} = [\theta_m, \Pi_i u_k^n]_0, \tag{21}$$

for any  $m = 1, \dots, 27$ , where terms of fixed point index  $r$  are computed by using the previous solution  $q_k^r$ . In our numerical tests, the fixed point iteration stops when the  $L^2(\hat{C})$ -norm of residual of equation (21) is less than a fixed tolerance.

In equation (17) the local map  $\mathcal{M}_i : \hat{C} \rightarrow \hat{C}_i^n$  has been involved for the computation of the local weak predictor solution. The local map is recovered through the movement of the foreground mesh led by the motion equation (3). Otherwise, namely in the background mesh, it is known *a priori*. The motion equation (3) is solved through an *isoparametric* approach by locally referring it to the same reference system as done for the local equation (12). This means that the spatial coordinates  $\mathbf{X}$  are considered as function of the reference coordinates, i.e.  $\mathbf{X}(\xi)$ , with  $\xi \in \hat{C}$ . Finally, the solution of the referred motion equation is approximated via a Lagrangian expansion by employing the same Lagrangian basis  $\{\theta_m\}_{m=1}^{27}$  built on the tensor combination of three Gauss-Legendre nodes in  $(0, 1)$  along any direction as previously introduced:  $\mathbf{X}_h = \theta_l \hat{\mathbf{X}}_l$ , with  $\hat{\mathbf{X}}_l = \mathbf{X}(\hat{\xi}_l)$ . Thus, from time  $t^n$  to  $t^{n+1}$ , the motion equation (3) is locally re-written as

$$\frac{d\mathbf{X}}{dt} = \mathbf{V} \text{ in } C_i^n, \tag{22}$$

and closed by strongly imposing that the solution  $\mathbf{X}^n$  at current time is equal to  $\mathbf{X}(t^n)$  found at the previous physical space-time cell  $C_i^{n-1}$ . The local motion equation (22) is weakened in a similar way to the local equation (12) and in algebraic form it reads

$$([\theta_m, \theta_l]_1 - \langle \partial_\tau \theta_m, \theta_l \rangle) \hat{\mathbf{X}}_l = \Delta t \langle \theta_m, \theta_l \rangle \hat{\mathbf{V}}_l + [\theta_m, \theta_l]_0 \hat{\mathbf{X}}_l^n, \tag{23}$$

for any  $m = 1, \dots, 27$ , with  $\hat{\mathbf{V}}_l = \mathbf{V}|_{\hat{\xi}_l}$ . The last term  $[\theta_m, \theta_l]_0 \hat{\mathbf{X}}_l^n$  takes into account the initial given configuration of the space at time  $t^n$ .

When the mesh is neither moving nor deforming, as for cells in the background, the mesh velocity is thus coincident with zero, i.e.  $\mathbf{V} \equiv \mathbf{0}$ . In that case, the map is known *a priori* and it consists in the rescaling of the reference space-time cell  $\hat{C}$  to the physical space-time cell  $C_i^n$ :

$$\begin{cases} x = x(\xi) = x_{i-1/2} + h_i^x \xi \\ y = y(\eta) = y_{i-1/2} + h_i^y \eta \end{cases}, \tag{24}$$

where coordinates  $x_{i-1/2}$  and  $y_{i-1/2}$  and  $x_{i+1/2}$  and  $y_{i+1/2}$  define the extremes along  $x$ - and  $y$ -direction of the physical space-time cell  $C_i^n \equiv [x_{i-1/2}, x_{i+1/2}] \times [y_{i-1/2}, y_{i+1/2}] \times [t^n, t^{n+1}]$ ; and  $h_i^x$  and  $h_i^y$  are the length along  $x$  and  $y$  of the cell, respectively, i.e.  $h_i^x = x_{i+1/2} - x_{i-1/2}$  and  $h_i^y = y_{i+1/2} - y_{i-1/2}$ .

Since the mesh motion equation (3) is essentially solved via a sort of Discontinuous Galerkin (DG) approach, possible numerical (and non physical) discontinuities could arise. As a matter of fact, for a given vertex  $\bar{\mathbf{X}}_j^{n+1}$  shared by a set of spatial cells  $\{\Omega_i^{n+1}\}_{i \in \mathcal{Z}_j^{n+1}}$  at time  $t^{n+1}$ , there could be as many different values of the vertex, namely  $\{\bar{\mathbf{X}}_{j,i}^{n+1}\}_{i \in \mathcal{Z}_j^{n+1}}$ , for any map  $\mathcal{M}_i$  referring to the cell  $C_i^n$  to which  $\Omega_i^{n+1}$  belongs. The set  $\mathcal{Z}_j^{n+1}$  collects the index(es) of the cells sharing the vertex  $\bar{\mathbf{X}}_j^{n+1}$ . The cardinality  $N_j$  of set  $\{\Omega_i^{n+1}\}_{i \in \mathcal{Z}_j^{n+1}}$ , coinciding with the cardinality of the indexes set  $\mathcal{Z}_j^{n+1}$ , depends on the position of the vertex  $\bar{\mathbf{X}}_j^{n+1}$  on the foreground mesh: it is either 1 or 2 if the vertex is on the boundary of the mesh,

otherwise it is 4, if the topology of the cell is quadrilateral. For this reason we consider a weighted average value for the shared vertex in order to tackle the possible arising discontinuities. As suggested in [53], we first consider a weighted velocity  $\bar{\mathbf{V}}_j^{n+1}$  corresponding to the vertex  $\bar{\mathbf{X}}_j^{n+1}$

$$\bar{\mathbf{V}}_j^{n+1} = \frac{1}{N_j} \sum_{i \in \mathcal{Z}_j^{n+1}} \bar{\mathbf{V}}_{j,i}^{n+1}, \text{ with } \bar{\mathbf{V}}_{j,i}^{n+1} = \int_0^1 \theta_l(\xi^*, \eta^*, \tau) d\tau \hat{\mathbf{V}}_{l,i}, \tag{25}$$

where coordinates  $(\xi^*, \eta^*)$  depend on the position of the coordinate  $\bar{\mathbf{X}}_j^{n+1}$  in the cell  $\Omega_i^{n+1}$ ; it can assume four values: (0, 0), (1, 0), (1, 1) and (0, 1). Once equation (23) is solved, the just found coordinates  $\{\hat{\mathbf{X}}_l\}_{l=1}^{27}$  are used for computing the velocity components  $\hat{\mathbf{V}}_{l,i}$  and, thus, the weighted velocities  $\bar{\mathbf{V}}_j^{n+1}$  in (25). Finally, the coordinates  $\bar{\mathbf{X}}_j^{n+1}$  at time  $t^{n+1}$  are

$$\bar{\mathbf{X}}_j^{n+1} = \bar{\mathbf{X}}_j^n + \Delta t \bar{\mathbf{V}}_j^{n+1}. \tag{26}$$

For another definition of the weighted vertex velocities  $\bar{\mathbf{V}}_j^{n+1}$  in (25) by exploiting the Voronoi neighborhood parameters of any vertex, the reader is addressed to [32].

In Algorithm 2 we resume the salient stages of the prediction step.

---

**Algorithm 2** Prediction step.

---

- 1: Compute the foreground mesh motion (26) from the motion equation (3) and through the weighted velocity (25);
  - 2: **for**  $i = 1, \dots, N$  **do**
  - 3: Find the map  $\mathcal{M}_i$  for the space-time cell  $C_i^n$ ;
  - 4: Compute (14), the Jacobian matrix  $J$  associated to  $\mathcal{M}_i$ ;
  - 5: Compute  $J^{-1}$  and take the submatrix  $J_s^{-1}$  as defined in (16);
  - 6: Update the convective-diffusive terms  $\mathcal{F}^v$  and  $\mathcal{F}^d$  in the reference domain;
  - 7: Evolve the local predictor solution through (20);
- 

4.1.2. The space-time finite volume scheme

Once the local predictor solution  $q_k$  is computed in each space-time cells  $C_i^n$ , we can perform the ADER correction stage. First, we rewrite the convective-diffusive equation (7) in divergence form. Let  $\mathbf{F}_{\mathbf{U}^n}(u_k^*, \nabla u_k^*) = \mathbf{U}^n u_k^* - \nabla u_k^*/\text{Re}$ , with  $k = 1, 2$ , be the convective-diffusion term associated to the component-wise equation (7); let  $\nabla_{\mathbf{x},t} = [\nabla, \partial_t]^T$  be the space-time differential operator and, finally, let  $\mathbf{U}_k = [\mathbf{F}_{\mathbf{U}^n}(u_k^*, \nabla u_k^*), u_k^*]^T$ ,  $k = 1, 2$ , be the  $k$ -component of the space-time solution, thus problem (7) can be rewritten as: for any  $k = 1, 2$ ,

$$\nabla_{\mathbf{x},t} \cdot \mathbf{U}_k = 0 \quad \text{in } \Omega(t) \times (0, T). \tag{27}$$

The objective is to find a finite volume solution for the above equation, where the finite volume is the space-time cell  $C_i^n$ , whose boundary reads

$$\partial C_i^n = \Omega_i^n \cup \Omega_i^{n+1} \cup \bigcup_{j=1}^4 \Gamma_{ij}^n, \tag{28}$$

where the boundaries  $\Gamma_{ij}^n$ ,  $j = 1, \dots, 4$ , are the space-time boundaries of  $C_i^n$  linking any edge of  $\Omega_i^n$  at time  $t^n$  to any edge of  $\Omega_i^{n+1}$  at time  $t^{n+1}$  (see the sketch of the physical space-time cell in Fig. 4). By integrating equation (27) over  $C_i^n$  and by applying the divergence theorem to the left side, we obtain

$$\oint_{\partial C_i^n} \mathbf{U}_k \cdot \mathbf{n}_{\mathbf{x},t} d\Gamma = 0, \tag{29}$$

with  $\mathbf{n}_{\mathbf{x},t} = [n_x, n_t]^T = [n_x, n_y, n_t]^T$  being the normal unit vector to the boundary  $\partial C_i^n$  of the cell. Let  $\bar{u}_{k,i}^{*,n}$  be the spatial average solution  $u_k^*$  cell-centered in the space cell  $\Omega_i^n$  at time  $t^n$ , i.e.,

$$\bar{u}_{k,i}^{*,n} = \frac{1}{|\Omega_i^n|} \int_{\Omega_i^n} u_k^*(x, y, t^n) dx dy, \tag{30}$$

where  $|\Omega_i^n|$  is the measure of the spatial cell  $\Omega_i^n$ . Though (28) and (30), equation (29) explicitly is

$$-|\Omega_i^n| \bar{u}_{k,i}^{*,n} + |\Omega_i^{n+1}| \bar{u}_{k,i}^{*,n+1} + \sum_{j=1}^4 \int_{\Gamma_{ij}^n} \mathbf{U}_k \cdot \mathbf{n}_{\mathbf{x},t} d\Gamma = 0, \tag{31}$$

where the unknown is the average solution  $\bar{u}_{k,i}^{*,n+1}$  at time  $t^{n+1}$ , while the last term of the left hand side is the space-time flux along the space-time sides  $\bigcup_{j=1}^4 \Gamma_{ij}^n$ . Scheme (31) is the space-time Finite Volume scheme; we remark that it is still exact. In order to solve (31), the integral function of the space-time flux is approximated through a Local Lax-Friederichs (LLF) approach:

$$[\mathbf{U}_k \cdot \mathbf{n}_{\mathbf{x},t}]_{\Gamma_{ij}^n} \approx \Phi(q_{k,j}^+, q_{k,j}^-) = \frac{1}{2}(\mathbf{U}_{k,j}^+ + \mathbf{U}_{k,j}^-) \cdot \mathbf{n}_{\mathbf{x},t} - \frac{s}{2}(q_{k,j}^+ - q_{k,j}^-), \tag{32}$$

where  $\mathbf{U}_{k,j}^+ = \mathbf{U}_{k,j}(q_{k,j}^+)$  and  $\mathbf{U}_{k,j}^- = \mathbf{U}_{k,j}(q_{k,j}^-)$  are the space-time solution of (27) computed by solutions  $q_{k,j}^+$  and  $q_{k,j}^-$ , which represent the local predictor solutions outside and inside the cell, respectively, with respect to the space-time side  $\Gamma_{ij}^n$ . The term  $s$  is the local stabilization coefficient depending on the face-centered velocity  $\mathbf{U}^n$  considered constant over the space-time side  $\Gamma_{ij}^n$ . It reads

$$s = \frac{1}{2} \left| \mathbf{U}^n \cdot \mathbf{n}_{\mathbf{x}} + 2n_t + \sqrt{\left[ (U_x^n)^2 + \frac{4}{\varepsilon \text{Re}} \right] n_x^2 + 2U_x^n U_y^n n_x n_y + \left[ (U_y^n)^2 + \frac{4}{\varepsilon \text{Re}} \right] n_y^2} \right|, \tag{33}$$

where  $\varepsilon$  is a relaxation parameter. In order to ensure a second-order convergence for the scheme, the relaxation term  $\varepsilon$  is chosen to be smaller than an optimal relaxation parameter  $\varepsilon_2$  [54,55] defined as

$$\varepsilon_2 = \frac{\mathcal{O}(1)h_{\max}^2}{C_2}, \tag{34}$$

where  $h_{\max}$  is the maximum characteristic length among all the cells and  $C_2 = (1 - 2^{-1/2})/(2^{-3/2} - 1)$  is a parameter depending on the convergence rate of the scheme. In particular, the relaxation parameter  $\varepsilon$  is set as  $\varepsilon_2/2$ . For further details concerning the stabilization term (33) and the stability of the scheme, the reader is referred to [36] and its references.

In the ADER scheme, flux is used to adjust information for contiguous cells. When overset meshes are employed, it also has the role of settling information from one block to the other along the fringe cells.

Equation (31) with the flux approximation (32) closes the correction stage of the ADER method. At the end of this stage, the cell-centered  $k$ -th component of the solution  $u_{k,i}^{*,n+1}$  is found over any cell  $\Omega_i^{n+1}$  at time  $t^{n+1}$ .

#### 4.2. The pressure equation

The second step of the fractional method is the projection step defined by the Poisson equation (10) for pressure  $\psi^{n+1} = \Delta t p^{n+1}$  at time  $t^{n+1}$  on the Chimera configuration for the domain  $\Omega^{n+1}$ . In this section, in order to lighten the notation, the reference to time  $t^{n+1}$  is omitted for all involved variables and quantities. Let the stencil  $\mathcal{S}_i$  centered on cell  $\Omega_i$  be decomposed in  $\mathcal{S}_i = \mathcal{S}_i^+ \cup \mathcal{S}_i^\times$ , with  $\mathcal{S}_i^+$  of cells sharing either one or no edge with  $\Omega_i$  and  $\mathcal{S}_i^\times$  the remaining cells sharing only one vertex of  $\Omega_i$ . The proposed scheme for (10) is a spatial FV approach. Thus, by integrating over the space cell  $\Omega_i$ , whose boundary is  $\partial\Omega_i = \bigcup_{j \in \mathcal{S}_i^+} \gamma_{ij}$ , and by applying the divergence theorem both to the left and right hand sides, the problem exactly reads

$$\sum_{j \in \mathcal{S}_i^+} \int_{\gamma_{ij}} \nabla \psi \cdot \mathbf{n}_{ij} d\gamma = - \sum_{j \in \mathcal{S}_i^+} \int_{\gamma_{ij}} \mathbf{U}^* \cdot \mathbf{n}_{ij} d\gamma, \tag{35}$$

with  $\mathbf{n}_{ij}$  the unit outer normal to side  $\gamma_{ij}$ . The integrals in (35) are approximated as

$$\sum_{j \in \mathcal{S}_i^+} |\gamma_{ij}| [\nabla \psi \cdot \mathbf{n}]_{ij} = - \sum_{j \in \mathcal{S}_i^+} |\gamma_{ij}| \mathbf{U}_{ij}^* \cdot \mathbf{n}_{ij}, \tag{36}$$

where  $|\gamma_{ij}|$  is the length of side  $\gamma_{ij}$ . In order to achieve the Poisson algebraic system for problem (36), the approximation of the face-centered normal divergence term  $[\nabla \psi \cdot \mathbf{n}]_{ij}$  along  $\gamma_{ij}$  is needed. For this reason, two different strategies are adopted with respect to the position of the spatial cell  $\Omega_i$ : if the cell is not *fringe*, namely it is not at the boundary of the overlapping interface of its partition, the approximation is performed through a *geometric* reconstruction, otherwise, an *analytic* approach is employed.

##### 4.2.1. The geometric reconstruction

By considering Fig. 5, let us consider two internal cells  $\Omega_1$  and  $\Omega_2$  in the same partition and sharing the edge  $\gamma$  of normal  $\mathbf{n}$ . Let  $P$  be the face-center of  $\gamma$ . Moreover, let  $\mathbf{c}_1$  and  $\mathbf{c}_2$  be the cell-centers of the two cells and  $\mathbf{v}_1$  and  $\mathbf{v}_2$  be the extremes of edge  $\gamma$ . These points define the unit direction vectors  $\mathbf{d}_c$  (of the centers) and  $\mathbf{d}_t$  (tangent), respectively. The objective is to approximate the normal gradient  $[\nabla \psi \cdot \mathbf{n}]_P$ , applied on  $P$ , assumed to be constant over  $\gamma$ . It is approximated via the *diamond formula* [37,38] as

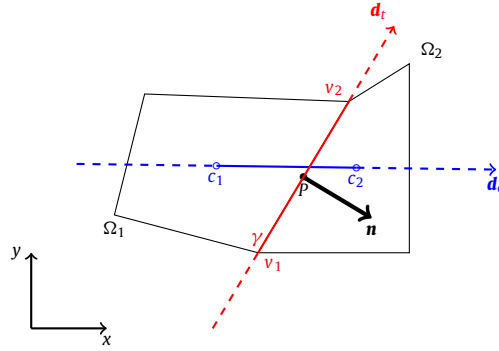


Fig. 5. Sketch of two internal cells  $\Omega_1$  and  $\Omega_2$  sharing the edge  $\gamma$ .

$$[\nabla \psi \cdot \mathbf{n}]_P \approx \frac{1}{\mathbf{d}_c \cdot \mathbf{n}} \left( \frac{\psi_{c_2} - \psi_{c_1}}{|\mathbf{c}_2 - \mathbf{c}_1|} - \frac{\psi_{v_2} - \psi_{v_1}}{|\gamma|} \mathbf{d}_c \cdot \mathbf{d}_t \right). \tag{37}$$

In the above approximation, due to the cell-centered nature of the scheme, an approximation of the vertex-centered quantities  $\psi_{v_1}$  and  $\psi_{v_2}$  are necessary. In particular, they have to be expressed as function of some cell-centered quantities of the unknown pressure  $\psi$ . Let us study this approximation for vertex  $\mathbf{v}_1$ ; the extension to vertex  $\mathbf{v}_2$  trivially follows. Let  $\tilde{S}_{v_1}$  be the substencil of indexes of those cells sharing vertex  $\mathbf{v}_1$ . For internal cells, the cardinality of substencil  $\tilde{S}_{v_1}$  is equal to 4. Thus, let  $\tilde{E}_{v_1} = \bigcup_{j \in \tilde{S}_{v_1}} \Omega_j$  be the subdomain composed of cells sharing the vertex  $\mathbf{v}_1$ . Finally, let  $\tilde{\Pi}_{v_1} \phi$  be the polynomial interpolation of a given function  $\phi \in C^2(\tilde{E}_{v_1})$ , whose knowledge is available to the cell-centers, by employing the bilinear basis of the polynomial space function  $\mathcal{Q}_1^0 = \text{span}\{1, x, y, xy\}$ . In particular, it holds that

$$\tilde{\Pi}_{v_1} \psi(x, y) = \alpha_{v_1,1} + \alpha_{v_1,2}x + \alpha_{v_1,3}y + \alpha_{v_1,4}xy = \mathbf{z}^T \boldsymbol{\alpha}_{v_1},$$

with  $\mathbf{z} = [1, x, y, xy]^T$  and the unknown polynomial coefficients collected in vector  $\boldsymbol{\alpha}_{v_1}$ . The polynomial coefficients are looked for by imposing that the polynomial equals the pressure at the cell-centers of the substencil (i.e.,  $\tilde{\Pi}_{v_1} \psi(x_j, y_j) \equiv \psi_j$  for any  $j$  in  $\tilde{S}_{v_1}$ ). This yields the resolution of linear system  $A_{v_1} \boldsymbol{\alpha}_{v_1} = \boldsymbol{\psi}_{v_1}$ , where the row space of  $A_{v_1} \in \mathbb{R}^{4 \times 4}$  is defined by the coordinates in  $\mathbf{z}_j$  and vector  $\boldsymbol{\psi}_{v_1}$  collects the cell-centered values  $\psi_j$ , with  $j \in \tilde{S}_{v_1}$ . Finally we approximate as follows:

$$\psi_{v_1} \approx \tilde{\Pi}_{v_1} \psi(x_{v_1}, y_{v_1}) = \mathbf{z}_{v_1}^T \boldsymbol{\alpha}_{v_1} = \mathbf{z}_{v_1}^T A_{v_1}^{-1} \boldsymbol{\psi}_{v_1}, \tag{38}$$

that only depends on cell-centered values of  $\psi$ . This allows to finally define the  $i$ -th line of system for problem (36). The scheme for internal cells reads

$$\sum_{j \in \mathcal{S}_i^+} \frac{|\gamma_{ij}|}{\mathbf{d}_{c_{ij}} \cdot \mathbf{n}_{ij}} \left( \frac{\psi_j - \psi_i}{|\mathbf{c}_j - \mathbf{c}_i|} - \frac{\mathbf{z}_{v_{2j}}^T A_{v_{2j}}^{-1} \boldsymbol{\psi}_{v_{2j}} - \mathbf{z}_{v_{1j}}^T A_{v_{1j}}^{-1} \boldsymbol{\psi}_{v_{1j}}}{|\gamma_{ij}|} \mathbf{d}_{c_{ij}} \cdot \mathbf{d}_{v_{ij}} \right) = \sum_{j \in \mathcal{S}_i^+} |\gamma_{ij}| \mathbf{U}_{ij}^* \cdot \mathbf{n}_{ij}, \tag{39}$$

where the unknowns are the cell-centered values of  $\psi$ .

#### 4.2.2. Truncation error and stencil at fringe cells

For the fringe cells, the diamond formula (37) for approximating the normal gradient in (35) is more complicated. In fact there exists at least one edge for which the second center  $\mathbf{c}_2$  falls in the other partition. Thus, in a generic configuration, it could be happen that the center direction  $\mathbf{d}_c$  tends to be parallel to the tangent direction  $\mathbf{d}_t$ , implying a vanishing term  $\mathbf{d}_c \cdot \mathbf{n}$ . The approach that we adopt exploits the analytic information stored in any stencil  $\mathcal{S}_i$  centered on cell  $\Omega_i$ . Let  $\mathcal{R}_i = \mathcal{S}_i \cup \{i\}$  be the increased stencil which includes also the index  $i$ . Let  $P$  the generic face-centered point on which the pressure gradient needs to be approximated. In the sequel we provide the gradient approximation along the  $x$ -direction; the approximation along  $y$  similarly follows. For any  $j$  in  $\mathcal{R}_i$ , the Taylor polynomial expansion of  $\psi_j$  with respect to the face-centered value  $\psi_P$  truncated to the third-order terms is

$$\begin{aligned} \psi_j = & \psi_P + h_j^x \partial_x \psi_P + h_j^y \partial_y \psi_P + h_j^x h_j^y \partial_{xy}^2 \psi_P + \frac{1}{2} (h_j^x)^2 \partial_{xx}^2 \psi_P + \frac{1}{2} (h_j^y)^2 \partial_{yy}^2 \psi_P \\ & + \frac{1}{6} (h_j^x)^3 \partial_{xxx}^3 \psi_P + \frac{1}{4} (h_j^x)^2 h_j^y \partial_{xxy}^3 \psi_P + \frac{1}{4} h_j^x (h_j^y)^2 \partial_{yyx}^3 \psi_P + \frac{1}{6} (h_j^y)^3 \partial_{yyy}^3 \psi_P + o(H_j^3), \end{aligned} \tag{40}$$

with  $h_j^x = x_j - x_P$ ,  $h_j^y = y_j - y_P$  and  $H_j = \max\{|h_j^x|, |h_j^y|\}$ . As done in the previous subsection, the objective is to represent the face-centered gradient as dependent on the cell-centered quantity in the stencil, i.e.,

$$\partial_x \psi_P = \sum_{j \in \mathcal{R}_i} \beta_{s_P(j)}^x \psi_j, \quad (41)$$

with coefficients  $\beta_{s_P(j)}^x$  to be found. The discrete function  $s_P : \mathcal{R}_i \rightarrow \{1, \dots, m\}$ , with  $m = |\mathcal{R}_i|$  being the cardinality of the enlarged stencil, sorts the indexes in  $\mathcal{R}_i$  in increasing order. By plugging the Taylor expansion (40) truncated to the second order in (41), it holds:

$$\begin{aligned} \partial_x \psi_P = & \left( \sum_{j \in \mathcal{R}_i} \beta_{s_P(j)}^x \right) \psi_P + \left( \sum_{j \in \mathcal{R}_i} \beta_{s_P(j)}^x h_j^x \right) \partial_x \psi_P + \left( \sum_{j \in \mathcal{R}_i} \beta_{s_P(j)}^y h_j^y \right) \partial_y \psi_P + \left( \sum_{j \in \mathcal{R}_i} \beta_{s_P(j)}^x h_j^x h_j^y \right) \partial_{xy}^2 \psi_P \\ & + \left( \sum_{j \in \mathcal{R}_i} \frac{1}{2} \beta_{s_P(j)}^x (h_j^x)^2 \right) \partial_{xx}^2 \psi_P + \left( \sum_{j \in \mathcal{R}_i} \frac{1}{2} \beta_{s_P(j)}^x (h_j^y)^2 \right) \partial_{yy}^2 \psi_P + \mathcal{O} \left( \max_{j \in \mathcal{R}_i} H_j^3 \right). \end{aligned} \quad (42)$$

Since the right side of (42) is the approximation of the  $x$ -derivative of  $\psi_P$ , the conditions on the coefficients  $\beta_{s_P(j)}^x$  are

$$\begin{aligned} \sum_{j \in \mathcal{R}_i} \beta_{s_P(j)}^x &= 0; & \sum_{j \in \mathcal{R}_i} \beta_{s_P(j)}^x h_j^x &= 1; & \sum_{j \in \mathcal{R}_i} \beta_{s_P(j)}^x h_j^y &= 0; \\ \sum_{j \in \mathcal{R}_i} \beta_{s_P(j)}^x h_j^x h_j^y &= 0; & \sum_{j \in \mathcal{R}_i} \frac{1}{2} \beta_{s_P(j)}^x (h_j^x)^2 &= 0; & \sum_{j \in \mathcal{R}_i} \frac{1}{2} \beta_{s_P(j)}^x (h_j^y)^2 &= 0; \end{aligned} \quad (43)$$

which can be synthesized in the linear system  $M\boldsymbol{\beta}^x = \mathbf{b}^x$ , with  $M \in \mathbb{R}^{6 \times m}$ ,  $\boldsymbol{\beta}^x \in \mathbb{R}^m$ ,  $\mathbf{b}^x \in \mathbb{R}^6$ . Similar consideration can be assumed for the approximation of the  $y$ -derivative. For this reason, for now we consider the generic system

$$M\boldsymbol{\beta} = \mathbf{b}. \quad (44)$$

Inspired by [39], for a general value of  $m$ , system (44) is solved by minimizing a Lagrangian function under the constraints defined by a convex function  $\mathcal{H} : \mathbb{R}^m \rightarrow \mathbb{R}$ . Let  $\boldsymbol{\lambda} \in \mathbb{R}^v$  be a vector of Lagrangian multipliers. Moreover let  $\mathcal{L} : \mathbb{R}^m \times \mathbb{R}^v \rightarrow \mathbb{R}$  be the Lagrangian function to be minimized defined as

$$\mathcal{L}(\boldsymbol{\beta}, \boldsymbol{\lambda}) = \mathcal{H}(\boldsymbol{\beta}) - \boldsymbol{\lambda}^T (M\boldsymbol{\beta} - \mathbf{b}). \quad (45)$$

To minimize this function means to find the stationary point  $(\boldsymbol{\beta}, \boldsymbol{\lambda})$  such that

$$\begin{cases} \frac{\partial \mathcal{L}}{\partial \boldsymbol{\beta}} = \mathbf{0} \\ \frac{\partial \mathcal{L}}{\partial \boldsymbol{\lambda}} = \mathbf{0} \end{cases} \iff \begin{cases} \frac{\partial \mathcal{H}}{\partial \boldsymbol{\beta}} - M^T \boldsymbol{\lambda} = \mathbf{0} \\ M\boldsymbol{\beta} = \mathbf{b} \end{cases}. \quad (46)$$

Let  $C \in \mathbb{R}^{4 \times m}$  be the sub-matrix relative to the second-order constraints (led by the second line of (40)). Two cases are distinguished:

$m \leq 10$ : The convex function is  $\mathcal{H}(\boldsymbol{\beta}) = 1/2 \boldsymbol{\beta}^T [(1 - \delta)C^T C + \delta G] \boldsymbol{\beta}$ , with  $v = 6$ , consequently the local system to be solved is

$$\begin{bmatrix} [(1 - \delta)C^T C + \delta G] & -M^T \\ M & O \end{bmatrix} \begin{bmatrix} \boldsymbol{\beta} \\ \boldsymbol{\lambda} \end{bmatrix} = \begin{bmatrix} \mathbf{0} \\ \mathbf{b} \end{bmatrix}, \quad (47)$$

where  $O$  is the null matrix in  $\mathbb{R}^{6 \times 6}$ . This choice of the convex function  $\mathcal{H}(\boldsymbol{\beta})$  is such that the discretization coefficients minimize the second-order truncation error encoded in matrix  $M$  and their  $L^\infty$ -norm is penalized by coefficient  $\delta$  (which is put equal to 0.01 in the presented test cases) in that region of the stencil indicated by matrix  $G \in \mathbb{R}^{m \times m}$ , as it will be later discussed.

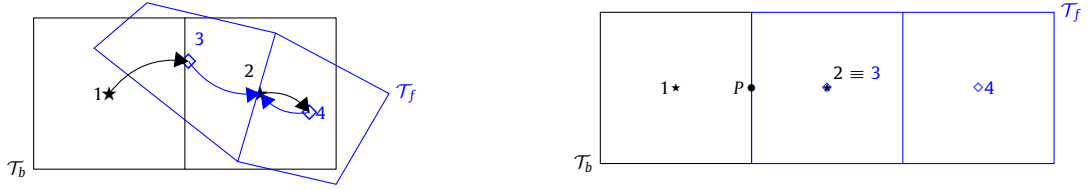
$m > 10$ : The convex function reads  $\mathcal{H}(\boldsymbol{\beta}) = 1/2 \boldsymbol{\beta}^T \boldsymbol{\beta}$  and  $v = 10$ . Thus the local minimization system is

$$\begin{bmatrix} I & -\tilde{M}^T \\ \tilde{M} & O \end{bmatrix} \begin{bmatrix} \boldsymbol{\beta} \\ \mathbf{0} \end{bmatrix} = \begin{bmatrix} \mathbf{0} \\ \mathbf{b} \end{bmatrix}, \quad (48)$$

with  $\tilde{M} = \begin{bmatrix} M \\ C \end{bmatrix}$  and  $I$  is the identity matrix in  $\mathbb{R}^{10 \times 10}$ . In this case the coefficients satisfy 10 second-order accuracy constraints while their norm is minimized.

The scheme for the fringe cells is

$$\sum_{j \in \mathcal{S}_i^+} |\gamma_{ij}| \sum_{l \in \mathcal{R}_i} (\beta_{s_{ij}(l)}^x n_{x,ij} + \beta_{s_{ij}(l)}^y n_{y,ij}) \psi_l = \sum_{j \in \mathcal{S}_i^+} |\gamma_{ij}| \mathbf{U}_{ij}^* \cdot \mathbf{n}_{ij}, \quad (49)$$



(a) In this configuration it holds:  $a_{bf}(\{1, 2\}) = \{3, 4\}$  while  $a_{fb}(\{3, 4\}) = \{2\}$ .

(b) No-shift configuration. It holds:  $a_{bf}(2) = 3 = a_{fb}^{-1}(2)$ ,  $a_{fb}(3) = 2 = a_{bf}^{-1}(3)$  and  $\Omega_2 \equiv \Omega_3$ .

**Fig. 6.** Sketch of overlapping configurations. Black cells  $\{1, 2\}$  belong to the background partitions, blue cells  $\{3, 4\}$  to the foreground. The star symbols (★) and the diamond symbols (◊) represent the cell-centers for cells in the background and in the foreground, respectively. To appreciate the figures at best, the reader is referred to the color electronic version of this paper.

where the unknowns are the cell-centered values of  $\psi$ .

Coefficients  $\beta^x$  and  $\beta^y$  in (49) automatically encode in the stiffness matrix of the Poisson problem (10) the information from one mesh to another since onto fringe cells the constructed stencils are hybrid (i.e., they are composed of cells belonging to the two partitions).

One goal for numerically solving the pressure problem is to have the same scheme for fringe and internal cells in the limit of a perfect no-shift overlapping between the background and foreground meshes. This allows to properly control the fluxes exiting from the background and entering in the foreground (and *vice versa*) and, consequently, to have a conservative scheme at least in this limit condition.

Let  $\mathcal{O}$  be the set of indexes for cells in the overlapping zone. It is possible to separate this set in two sets  $\mathcal{O}_b$  and  $\mathcal{O}_f$  for the background and foreground, respectively, such that  $\mathcal{O} = \mathcal{O}_b \cup \mathcal{O}_f$  and  $\mathcal{O}_b \cap \mathcal{O}_f = \emptyset$ . Moreover, let  $a_{bf} : \mathcal{O}_b \rightarrow \mathcal{O}_f$  (and  $a_{fb} : \mathcal{O}_f \rightarrow \mathcal{O}_b$ ) be the function associating the closest background (foreground) overlapping cell to a given foreground (background) overlapping cell, i.e., for any  $i \in \mathcal{O}_b$  (and  $j \in \mathcal{O}_f$ )

$$a_{bf}(i) = \arg \min_{j \in \mathcal{O}_f} |\mathbf{x}_i - \mathbf{x}_j| \quad \left( \text{and } a_{fb}(j) = \arg \min_{i \in \mathcal{O}_b} |\mathbf{x}_j - \mathbf{x}_i| \right). \quad (50)$$

In a general overlapping configuration, it holds that  $a_{fb}^{-1} \neq a_{bf}$  and  $a_{bf}^{-1} \neq a_{fb}$ , as it is showed in Fig. 6a. Through the association functions it is possible to formalize the no-shift overlapping limit configuration.

**Definition 4.1** (*No-shift overlapping configuration*). The overlapping configuration is said to be no-shift when it holds both

$$a_{bf} = a_{fb}^{-1} \quad \text{or} \quad a_{fb} = a_{bf}^{-1}; \quad (51a)$$

$$\forall i \in \mathcal{O}_b \quad \exists ! j = a_{bf}(i) \in \mathcal{O}_f \quad \text{such that} \quad i = a_{fb}(j) \quad \text{and} \quad \overline{\Omega_i \cap \Omega_j} = \overline{\Omega_k}, \quad \text{with } k = i, j. \quad (51b)$$

The limit of no-shift condition takes place when all overlapping cells in the background perfectly coincide with all overlapping foreground cells in the foreground with a one-to-one match defined by the associations functions (an example is sketched in Fig. 6b).

Let us consider a fringe cell  $\Omega_i$  in a no-shift overlapping configuration for uniform Cartesian meshes of characteristic length  $h$  and let us suppose to compute the gradient at the face-center  $P$  of the side after which there is cell  $\Omega_j$  not belonging to the same partition of  $\Omega_i$  (as in Fig. 6b for cells  $\Omega_3$ , fringe, and  $\Omega_1$ , internal). If the diamond formula (37) is used in this case, the tangential contribution vanishes because  $\mathbf{d}_c \cdot \mathbf{d}_t = 0$ , consequently, the diamond formula corresponds to the minimization of the Lagrangian functional associated to problem (44) fulfilling the second-order constraints (43) with coefficients:  $\beta_{s_{ij}(i)} = -\beta_{s_{ij}(j)} = -1/h$  and  $\beta_{s_{ij}(k)} = 0$  for any  $k \in \mathcal{R}_i / \{i, j\}$ . This means that the diamond formula in the view of the problem defined by (47) is minimizing the  $L^\infty$ -norm of the local parameters only in those cells of the stencil sufficiently far from the face-center point  $P$  (where the value of the local coefficients is put to 0). Consequently, all the information for the reconstruction of the gradient is recovered from the closest cells to  $P$ . This concept is encoded in matrix  $G$  defined as a diagonal matrix  $G = \text{diag}(g_{s_{ij}(k)})_{k \in \mathcal{R}_i}$ , with the diagonal components defined as

$$g_{s_{ij}(k)} = \begin{cases} 1; & k \neq \arg \min_{l \in \mathcal{R}_i} |\mathbf{x}_l - \mathbf{x}_P| \\ 0; & \text{otherwise} \end{cases}. \quad (52)$$

With this definition, in the considered overlapping configuration, components  $g_k$  assume value 1 only for  $k \neq i, j$  (thus for all cells whose centers do not minimize the distance with the face-center  $P$ ) and the solution of problem (47) can be proved to provide  $\beta_{s_{ij}(i)} = -\beta_{s_{ij}(j)} = -1/h$  and  $\beta_{s_{ij}(k)} = 0$  for any  $k \in \mathcal{R}_i / \{i, j\}$ , as defined by the diamond formula. When matrix  $G$  is put equal to the identity, the  $L^\infty$ -norm is penalized all over the stencil [39]. In the simulations of this work, matrix  $G$  with coefficients defined by (52) is used for any overlapping configuration, allowing to have a unique scheme for internal and fringe cells in the limit of the no-shift overlapping condition.

### 4.3. The face-center discrete operators on overset grids

Accordingly to the Chorin-Temam scheme presented at the beginning of Section 4, the face-centered values of the velocity and pressure gradient are needed. These computations take again into account either the internal or fringe position of the cell.

When the intermediate velocity  $\mathbf{u}^*$  is computed at the end of the predictor step (7), its face-centered counterpart  $\mathbf{U}^*$  becomes the force term for the pressure equation (10). If the edge is shared by two cells of the same partition, the face-centered approximation is the mean of the  $\mathcal{P}_2$ -interpolations evaluated on the face-center by using both the stencils of the two involved cells. On the contrary, when the side only belongs to one cell (because it is fringe), the approximation is still the evaluation of the polynomial interpolation on the face-center but just considering the hybrid stencil of the cell.

In the last step (11b) of the fractional step, the face-centered gradient pressure is used to correct the new face-centered velocity. For fringe cells, the face-centered approximation still exploits the local coefficients explained in the Section 4.2.2. For internal cells, through the diamond formula (37), it is possible to approximate the directional derivatives on the face-center along the center and tangential directions. In particular they read

$$\partial_{\mathbf{d}_c} \psi \approx \frac{\psi_{c_2} - \psi_{c_1}}{|\mathbf{c}_2 - \mathbf{c}_1|} \quad \text{and} \quad \partial_{\mathbf{d}_t} \psi \approx \frac{\psi_{v_2} - \psi_{v_1}}{|\gamma|}, \tag{53}$$

respectively, where  $\partial_{\mathbf{d}} \psi = \nabla \psi \cdot \mathbf{d}$  is the directional derivative of  $\psi$  along direction  $\mathbf{d}$ . Consequently it holds

$$\begin{bmatrix} d_{c,x} & d_{c,y} \\ d_{t,x} & d_{t,y} \end{bmatrix} \begin{bmatrix} \partial_x \psi \\ \partial_y \psi \end{bmatrix} = \begin{bmatrix} \partial_{\mathbf{d}_c} \psi \\ \partial_{\mathbf{d}_t} \psi \end{bmatrix} \tag{54}$$

which can be compactly written in an algebraic form as  $D(\nabla \psi)_{fc} = \mathbf{w}$ . By solving the local face-centered system (54), correction (11b) is finally performed.

### 4.4. Dynamics of the overlapping zone

During the simulation, the foreground mesh moves and, consequently, the background mesh changes its configuration in the zone of the overlapping as well as in the hole. Let  $\Omega_i(t)$  be a background cell in a neighborhood of the overlapping. From times  $t^n$  to  $t^{n+1}$ , it can happen one of the following three scenarios:

1. Cell  $\Omega_i(t)$  is present at time  $t^n$  and it disappears at time  $t^{n+1}$  because the hole completely covers it;
2. Cell  $\Omega_i(t)$  is not present at time  $t^n$  but it appears at time  $t^{n+1}$  because the hole gets away;
3. The overlapping zone does not drastically change its configuration with respect to cell  $\Omega_i(t)$ , thus the cell is present at time  $t^n$  and it still continues to be present at time  $t^{n+1}$ .

The third case is trivial. For the first case, the algorithm is performed on the vanishing cell because of the computation of fluxes needed by the neighboring cells and at time  $t^{n+1}$  the cell (with data) is suppressed. For the second possibility, information at current time  $t^n$  is missing and it is necessary for evolving the same information at next time  $t^{n+1}$ . By recalling the previously introduced notation, in this case index  $i$  belongs to the overlapping background set  $\mathcal{O}_b$ . Thus, it is possible to associate to it an index  $j = a_{bf}(i)$  in the foreground set  $\mathcal{O}_f$  such that information stored in  $\Omega_j^n$  is known. Successively, a  $\mathcal{P}_2$ -reconstruction evaluated on  $\Omega_i$  is employed by using the stencil  $\mathcal{S}_j$  of  $\Omega_j^n$ . Since there are several layers of cells composing the overlapping zone, this ensures stencil  $\mathcal{S}_j$  to be entirely defined in the foreground partition and, consequently, the reconstructed data do not need information coming from the other partition where possibly there is the new born cell  $\Omega_i$ , namely where data themselves want to be approximated. Finally, the algorithm is performed as usual.

## 5. Numerical results

In Section 5.1 the performances of the algorithm with respect to the order of grid convergence are presented. In Sections 5.2 and 5.3 validations of physical data for simulations of lid driven cavity and flows around cylinders, respectively, compared to the literature are presented.

### 5.1. Order of convergence

For measuring the order of convergence of the method we computed the  $L^2$ - and  $L^\infty$ -norms of the mismatch between the numerical solutions (both velocity and pressure) and the exact ones ( $\mathbf{u}_{ex}$ ,  $p_{ex}$ ) for the Taylor-Green vortexes in the computational domain  $\Omega = (-\pi, \pi)^2$  at final time  $T = 1$ . The exact solution of this problem reads:

$$\mathbf{u}_{ex}(x, y, t) = \begin{bmatrix} \cos(x) \sin(y) \exp(-2vt) \\ -\sin(x) \cos(y) \exp(-2vt) \end{bmatrix}; \quad p_{ex}(x, y, t) = -\frac{\rho}{4} (\cos(2x) + \sin(2y)) \exp(-4vt),$$

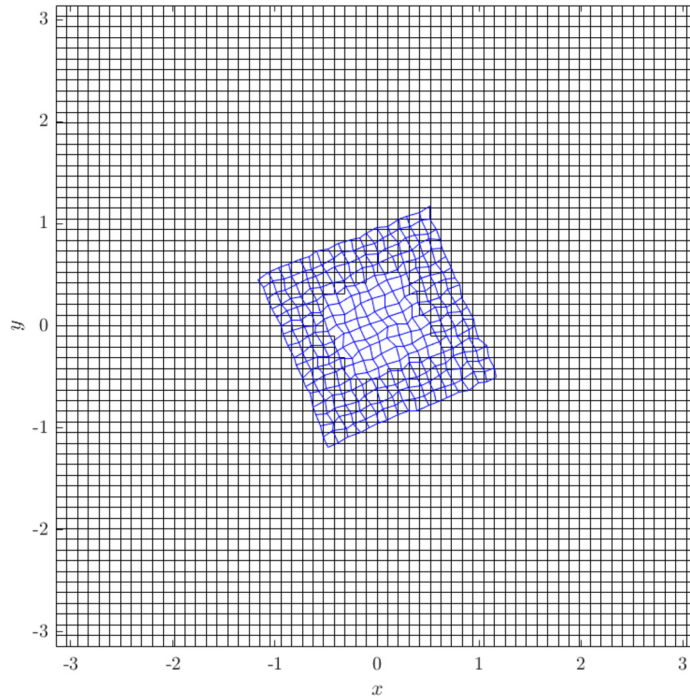
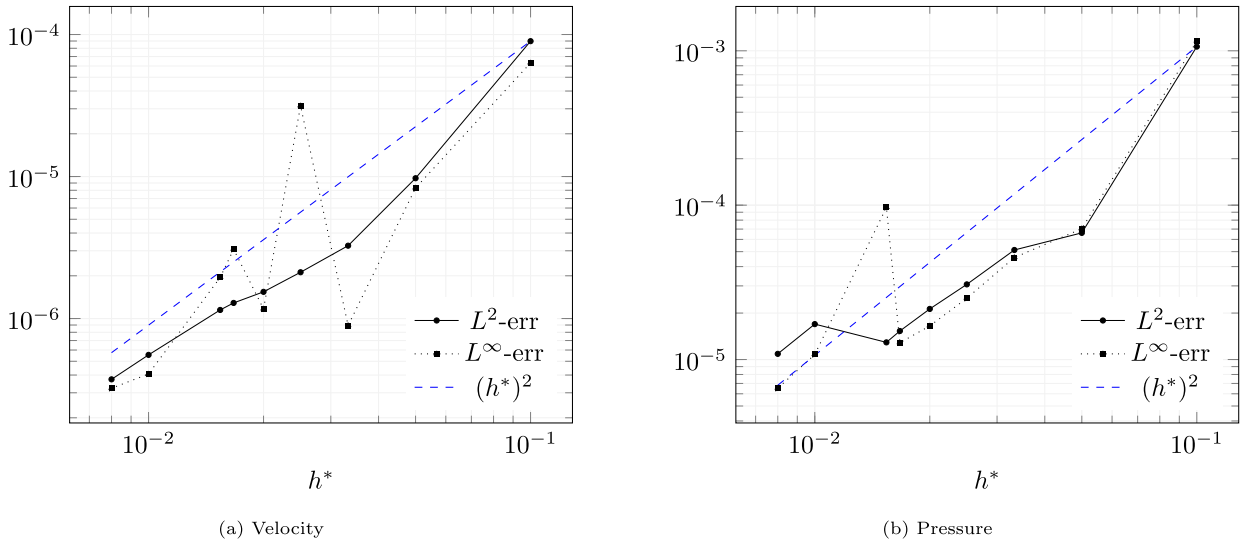


Fig. 7. Initial mesh configuration for Taylor-Green vortex.

with  $\nu = 10^{-2}\pi$  and  $\rho = 1$ . The foreground mesh originally covers the subdomain defined by a square of length  $\pi/4$  centered in the origin and inclined of  $\pi/8$ . It is originally built by a structured mesh of cells of the same characteristic dimension  $h$  of cells in the background; successively, any of its vertices is randomly perturbed of a maximum length of  $h/2$  (see Fig. 7). Moreover, it rigidly counterclockwise rotates around the origin of axes accordingly to the mesh velocity  $\mathbf{V} = 1/2[-y, x]^T$ . At the boundaries, the numerical velocity is imposed to be equal to the exact solution. In order to measure the space-time order of convergence, the time step  $\Delta t$  is chosen by respecting the CFL condition; in particular, since at the boundaries the maximum velocity is 1, we set  $\Delta t = \text{CFL}h/u_\infty$ , with  $\text{CFL} = 0.4$  and  $u_\infty = 1$ . The studied problem is nondimensionalized by a characteristic length  $L = \pi$ ; consequently the Reynolds number is  $\text{Re} = 100$ . By looking at Fig. 8, the  $L^2$ -norm convergence rate for both velocity and pressure is approximately 2; the  $L^\infty$ -norm trend does not follow any a priori definable convergence. It is inferred that uniform convergence does not occur as the mesh size decreases, but globally the number of cell-centers that cause this to occur is much less than for the rest of the nodes.

## 5.2. The lid driven cavity

In this section we study a lid driven cavity flow at  $\text{Re} = 1000$ . At the initial time the fluid has zero velocity inside the cavity  $\Omega = (0, 1)^2$ . No slip conditions (i.e.,  $\mathbf{u} \equiv \mathbf{0}$ ) are strongly imposed on all sides of the cavity with exception to the upper boundary where velocity is constant and equal to  $[-1, 0]^T$ . A steady foreground mesh occupies the subdomain  $(0.21, 0.79)^2$ . Both the background and the foreground meshes are uniform and Cartesian, with a characteristic length  $h = 1/128$ . Moreover the overlapping configuration is no-shift. We are interested in the steady solution. This solution is reached when the  $L^2$ -norm of the difference between the solutions at two consecutive times  $t^n$  and  $t^{n+1}$  is less than  $10^{-10}$ . Fig. 9 shows the streamlines at the steady state. The solution presents a main vortex and two minor vortices located towards the lower corners of the cavity. The main vortex originates from the upper boundary and moves to the region discretized by the foreground mesh. In order to quantitatively measure this movement, we consider the geometrical topological point where the stream-function  $\Psi$  is maximized. Before the steady condition, this topological point moves from the background to the foreground by passing through the overlapping zone. Table 1 resumes the comparison of the maximum stream-function  $\Psi_{\max}$  and its location. Along the topological point, also the value of the vorticity  $\omega$  is reported. All data from the literature for the comparison consider a discretization grid of  $128 \times 128$ . The validation confirms that the presence of the foreground mesh does not influence the performance of the simulation. The results are in good agreements with reference ones. No perturbations to the numerical solution are induced by the foreground mesh in the case of no-shift overlapping condition. Moreover, due to the no-shift overlapping configuration, on the overlapping zone stream-function and vorticity in background are identical to the stream-function and vorticity in foreground, respectively.



**Fig. 8.** Convergence analysis for Taylor-Green Vortices in  $(-\pi, \pi)^2$  at final time  $T = 1$  with respect to the nondimensionalized mesh size  $h^* = h/L$  for velocity (a) and pressure (b). The errors are in norms  $L^2$  and  $L^\infty$ .

**Table 1**

Comparison on the primary vortex for the lid driven cavity: maximum stream-function  $\Psi_{\max}$ , vorticity  $\omega$  and location of the topological point. The reference into brackets indicates the used methodology.

	$\Psi_{\max}$	$\omega$	$x$	$y$
Present	0.1171	1.9721	0.4687	0.5625
Bruneau [56]	0.1179	2.0508	0.4687	0.5625
Bruneau [56] (Upwind)	0.1180	2.0549	0.4687	0.5625
Bruneau [56] (Kawamura [57])	0.1179	2.0557	0.4687	0.5625
Bruneau [56] (Quickest [58])	0.1150	1.9910	0.4687	0.5625
Ghia [59]	0.1179	2.0497	0.4687	0.5625

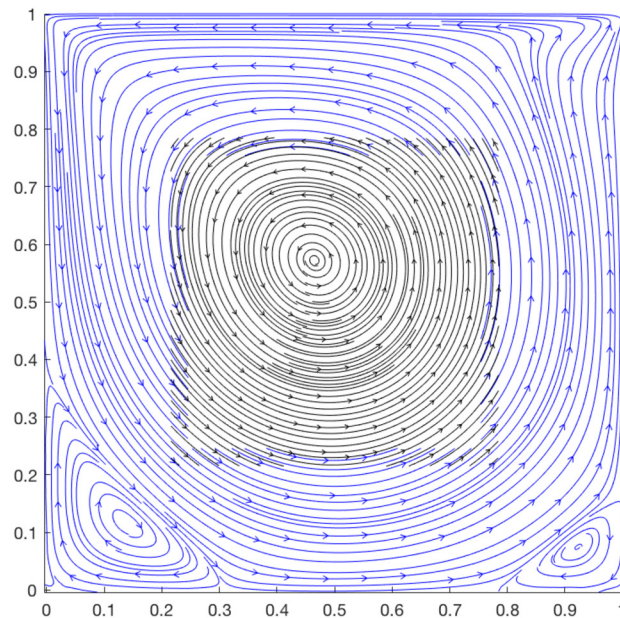


**Fig. 9.** Steady streamlines for the lid driven cavity test: blue for the background and black for the foreground. To appreciate the figures at best, the reader is referred to the color electronic version of this paper.

**Table 2**

Features of the five considered Chimera meshes for the convergence grid study. The number of cells in background and foreground are  $N_b$  and  $N_f$ , respectively, whose sum is  $N$ . Label  $N_B$  refers to the number of cells around the cylinder, namely the number of cells in the first inner layer discretizing the boundary of the cylinder.

	Background		Foreground			$N$	
	$h$	$N_b$	min( $h$ )	max( $h$ )	$N_f$		$N_B$
<i>Grid1</i>	4.00e-1	2604	2.14e-2	4.00e-1	2686	80	5290
<i>Grid2</i>	3.00e-1	4510	1.11e-2	3.00e-1	4554	100	9044
<i>Grid3</i>	3.00e-1	4510	7.90e-3	3.00e-1	7848	110	12358
<i>Grid4</i>	2.00e-1	10004	7.90e-3	2.00e-1	7194	110	17198
<i>Grid5</i>	1.00e-1	39204	6.90e-3	1.00e-1	18183	210	57387

### 5.3. The cylinders

In this section the method is validated by studying the flow around a cylinder that can be steady or moving. We refer the reader to [60] for a more specific numerical scheme for the study of the movement of the spheres embedded in an incompressible fluid with use of overset grids. In particular, in this work, the Navier-Stokes equations are solved in spherical coordinates onto the foreground mesh and the information exchange between the different blocks is performed by third-order Lagrangian interpolation for both velocity and pressure.

Let  $\mathbf{u}_\infty$  be the fluid velocity at the inlet boundary of the computational domain. Moreover we recall that  $\mathbf{u}_B$  is the body velocity (i.e. of the cylinder). Let the dimensionless stress tensor  $\mathbb{T}(\mathbf{u}, p)$  be defined as

$$\mathbb{T}(\mathbf{u}, p) = -pI + \frac{1}{\text{Re}}(\nabla\mathbf{u} + \nabla\mathbf{u}^T), \quad (55)$$

with  $I$  the identity tensor. The fluid dynamics force  $\mathbf{F}_f$  and torque  $M_f$  exerted by the fluid on the cylinder are

$$\mathbf{F}_f = \oint_{\partial\Omega_B} \mathbb{T}(\mathbf{u}, p)\mathbf{n}_B \, d\gamma_B, \quad (56a)$$

$$M_f = \oint_{\partial\Omega_B} \mathbf{r}_B \wedge \mathbb{T}(\mathbf{u}, p)\mathbf{n}_B \, d\gamma_B, \quad (56b)$$

where  $\mathbf{n}_B$  is the unit outer normal to the cylinder and  $\mathbf{r}_B$  is the position of any point along the boundary  $\partial\Omega_B$  of the cylinder. We define the aerodynamics coefficients as  $\mathbf{C} = 2\mathbf{F}_f/(\rho u_\infty^2 D)$ , with  $D$  the diameter of the cylinder and  $u_\infty = \|\mathbf{u}_\infty\|$ . Finally, let the drag  $C_D$  and lift  $C_L$  coefficients be  $C_D = \mathbf{C} \cdot \mathbf{e}_x$  and  $C_L = \mathbf{C} \cdot \mathbf{e}_y$ , respectively, with  $\{\mathbf{e}_x, \mathbf{e}_y\}$  the canonical basis for  $\mathbb{R}^2$ .

The geometrical setting in this section is the same for all test cases. For this reason we study the grid convergence on one case and we consider the same set of back- and foreground meshes for all the other test cases. This test case simulates the flow around a steady cylinder at  $\text{Re} = 550$  with an inlet fluid velocity  $\mathbf{u}_\infty = [1, 0]^T$ . The center of the cylinder is located in the origin of the axis and is  $8D$  far from the inlet boundary,  $16D$  from the outlet boundary and  $8D$  from any of the upper and lower boundary of the channel. At the boundaries, at the inlet a constant velocity  $\mathbf{u}_\infty$  is imposed, there are no-reflecting conditions at the outlet [61] and streamline conditions (i.e.,  $v = 0$  and  $\partial_y u = 0$ ) on the other two boundaries. Since the analytical solution for this case is not available, we compute the drag coefficient evolution in the time window  $[0, 5]$  for five different Chimera grid configurations, resumed in Table 2. *Grid1* is the coarsest grid and *Grid5* is the finest one. In particular, *Grid3* is an intermediate configuration between *Grid2* and *Grid4*. In fact it mixes the background characteristics of *Grid2* with the foreground ones of *Grid4*. The drag coefficients from the different overset configurations are also compared with the one by Ploumhans and Winkelmanns [62] for the same test case. Fig. 10 shows the comparison. All curves match the one from the literature and, from the second to the last configuration, the drag coefficient is the same. For this reason we use the Chimera mesh *Grid3* (in Fig. 11) because, among all the meshes, it allows a good compromise between computational times and numerical results.

#### 5.3.1. Steady cylinder

Let us consider the same configuration of the steady cylinder test case for a Reynolds number  $\text{Re} = 200$ . In particular we study the asymptotic regime (long time integration). For this test case the validation with literature is performed for the average drag coefficient and the Strouhal number  $S_t = f_v D / u_\infty$ , with  $f_v$  the frequency of vortex shedding. The comparison in Table 3 shows that the results obtained with the presented scheme match the results of the literature. In Fig. 12 there are the plots of the drag and lift coefficients for the whole time period of integration.

#### 5.3.2. Impulsively started cylinders

We now consider the impulsively started cylinders, namely test cases for which  $\mathbf{u}_B \neq \mathbf{0}$  and  $\mathbf{u}_\infty = \mathbf{0}$ . In this case no reflecting conditions are imposed also on the inlet boundary. At the initial time the cylinder is horizontally shifted of  $5D$

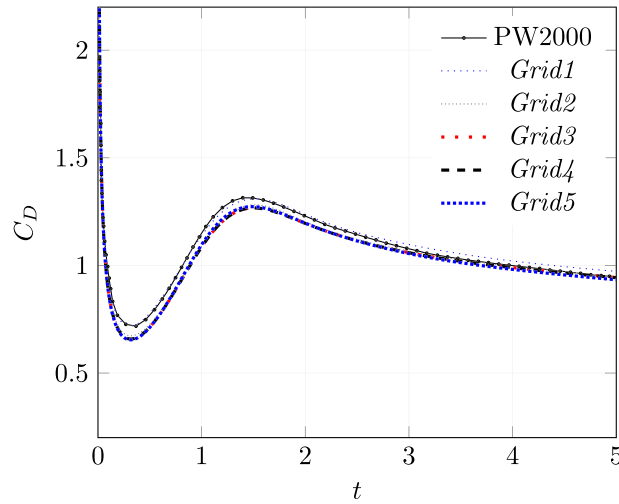


**Fig. 10.** Drag coefficient for the zero test case (steady cylinder at  $Re = 550$ ). The comparison is also validated with the drag coefficient from Ploumhans and Winkelmanns (PW2000) [62].

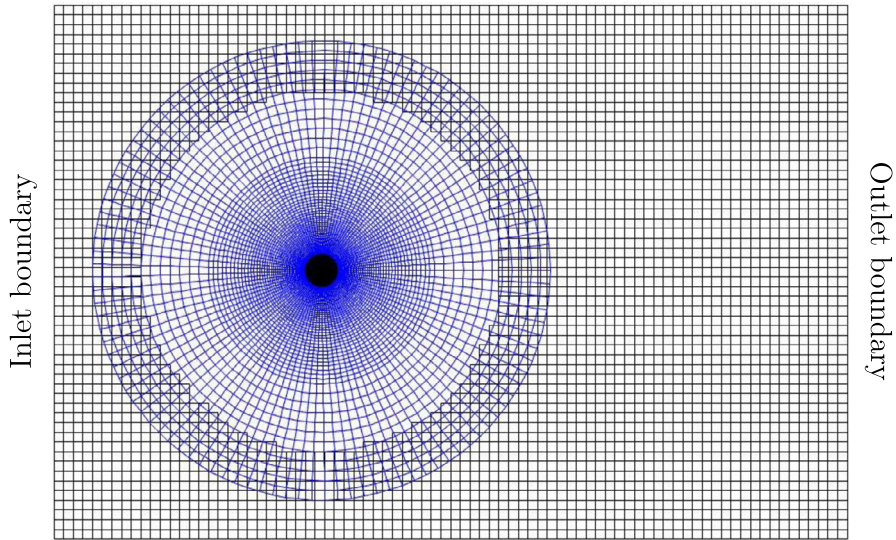


**Fig. 11.** Chimera configuration of *Grid3*. The diameter of the cylinder is  $D$  and the maximum diameter of the foreground mesh is  $10D$ . In background, the hole as a diameter of  $\sim 7.4D$ .

**Table 3**

Comparison for the average drag coefficient  $C_D$  and the Strouhal number  $S_f$  for the steady cylinder at  $Re = 200$ .

	$C_D$	$S_f$
Present	1.3430	0.1979
Bergmann [63]	1.3900	0.1999
Bergmann Iollo [64]	1.3500	0.1980
Bergmann et al. [65]	1.4000	-
Braza et al. [66]	1.4000	0.2000
He et al. [67]	1.3560	0.1978
Henderson [68]	1.3412	0.1971

towards the outlet boundary with respect to the steady test cases. For the whole time interval of integration a constant velocity  $\mathbf{u}_\infty = [-1, 0]^T$  is imposed to the cylinder.

In these conditions, at  $Re = 550$  we expect a similar situation with the zero test case. Thus we compute the drag coefficient by comparing it to both the one of the steady case and the one from the literature provided by Ploumhans and Winkelmanns [62] as previously done. The comparison is plotted in Fig. 13. The curves for the steady and moving cases are

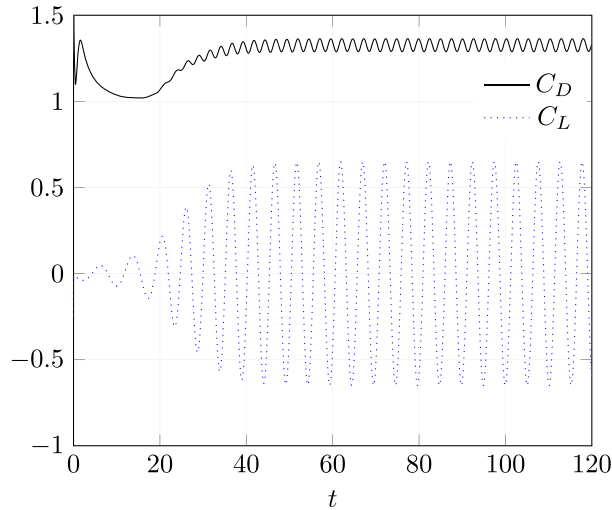


Fig. 12. Drag and lift coefficients for the steady cylinder at  $Re = 200$ .

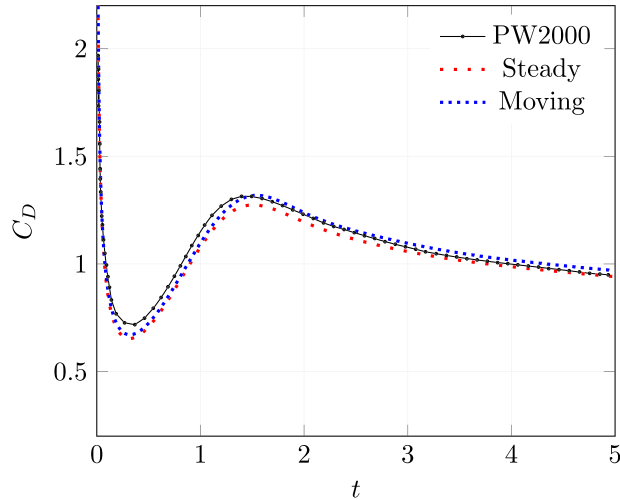


Fig. 13. Comparison of drag coefficient between the steady and impulsively started cylinder at  $Re = 550$ . Both are compared with the results by Ploumhans and Winckelmans (PW2000) [62].

very similar and comparable with the reference literature data. The similarity of the two test cases is also evident from the color plots of the pressure at the same time  $t = 5$  in Fig. 14.

As for the steady test cases, we also considered the impulsively started cylinder at  $Re = 200$ . By analyzing the comparison in Fig. 15 of the drag coefficient and data from the literature by Koumoutsakos and Leonard (KL1995) [69] and Bergmann et al. (BHI2014) [65], there is a good agreement with the previous studies.

### 5.3.3. Impulsively started then stopped cylinders

With the same boundary conditions of the previous subsection, we also consider test cases where the cylinder is impulsively starting its movement and at a given time  $t_0$  it stops. For this subsection we consider a viscous-dominant flow at  $Re = 40$  and a convective-dominant flow at  $Re = 550$ . For the former case the stopping time  $t_0 = 5$ , while in the latter case the cylinder is stopped at  $t_0 = 2.5$ . For both cases, before stopping, the cylinder has a constant velocity  $\mathbf{u}_B = [-1, 0]^T$ . Figs. 16 and 17 show the plot of the evolution of the drag coefficient compared with data from literature provided by Koumoutsakos and Leonard [69] and Bergmann et al. [65] for both test cases. Also in this case present data match the previous studies.

With the same accuracy, evaluated against the test cases of Bergmann et al. [65], the validated data though the presented method require the mesh to be composed of a number of cells from 1 to 2 orders of magnitude less. As a matter of fact, if the degrees of freedom in [65] and [64] are  $\sim 10^6$  and  $\sim 10^5$ , respectively, the overset grid exploits  $\sim 10^4$  spatial cells.

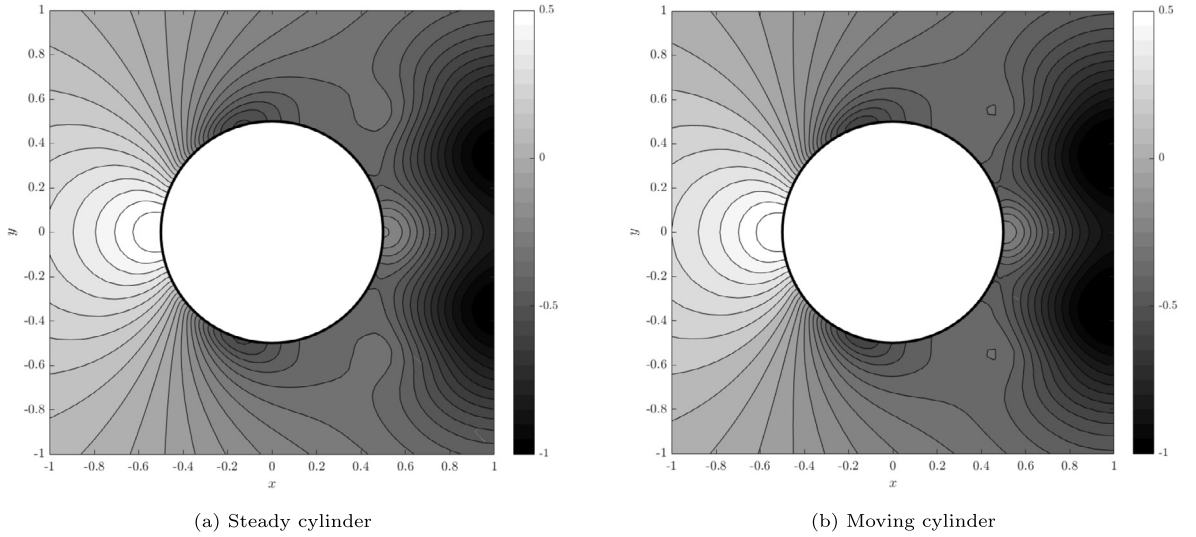


**Fig. 14.** Pressure at  $t = 5$  for steady and impulsively moving cylinders at  $Re = 550$ .

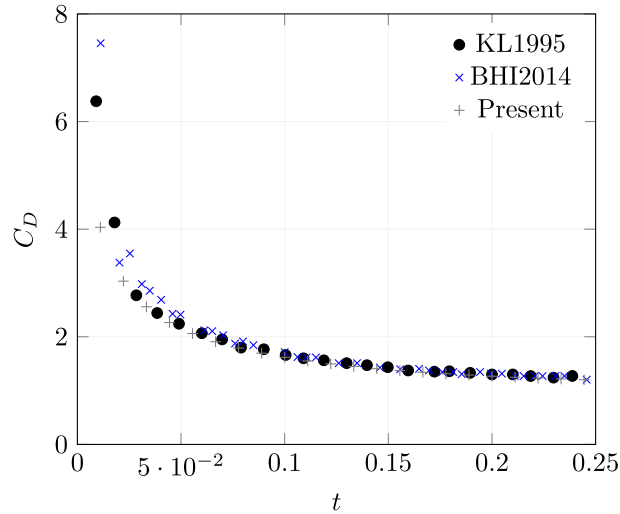


**Fig. 15.** Comparison of the evolution of the drag coefficient up to  $t = 0.25$  for the impulsively started cylinder at  $Re = 200$  with data by Koumoutsakos and Leonard (KL1995) [69] and Bergmann et al. (BHI2014) [65].

## 6. Sedimentation of a cylinder

The last test case analyzes the sedimentation of a cylinder in a cavity. In order to validate the computed data with the proposed method, we set the same configuration by Coquerelle and Cottet [70], Bergmann et al. [65] and Bergmann and Iollo [64]. The cavity is defined by the vertical channel  $[0, 2] \times [0, 6]$  with a two-dimensional cylinder, with its center of mass originally located in  $(1, 4)$ , falls subjected to the gravity up to the lower boundary. The cylinder radius is  $r = 0.125$  with a density  $\rho_s = 1.5$ . The viscosity and the density of the bounding fluid are  $\nu = 0.01$  and  $\rho_f = 1.0$ , respectively. The gravity has a modulus  $g = -980$ . The cylinder moves accordingly to

$$\mathbf{u}_B = \mathbf{V} + \boldsymbol{\Omega} \wedge (\mathbf{x} - \mathbf{x}_G), \quad (57a)$$

$$m_B \dot{\mathbf{V}} = -\mathbf{F}_f + \tilde{m} \mathbf{g}, \quad (57b)$$

$$J_B \dot{\boldsymbol{\Omega}} = M_f, \quad (57c)$$

where  $\mathbf{V}$  and  $\boldsymbol{\Omega}$  are the translation and rotational velocities, respectively, and  $\mathbf{x}_G$  is the center of the cylinder; in the translation equation (57b)  $m_B = \pi r^2 \rho_s$  is the cylinder mass while  $\tilde{m} = \pi r^2 (\rho_s - \rho_f)$  is the difference of fluid and cylinder

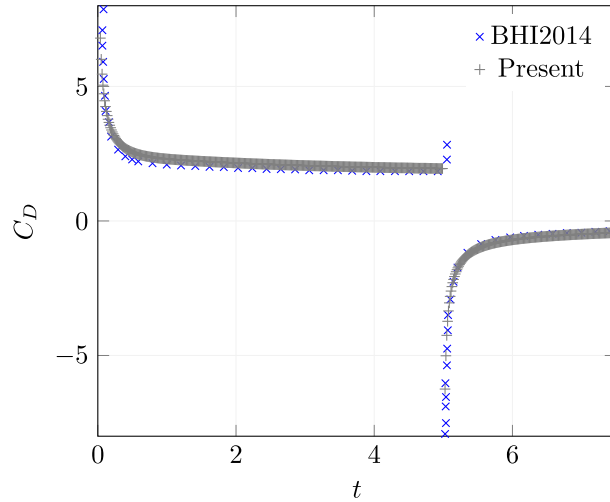


Fig. 16. Comparison of the evolution of the drag coefficient up to  $t = 7.5$  for the impulsively started and then stopped cylinder at  $Re = 40$  with data by Bergmann et al. (BHI2014) [65].

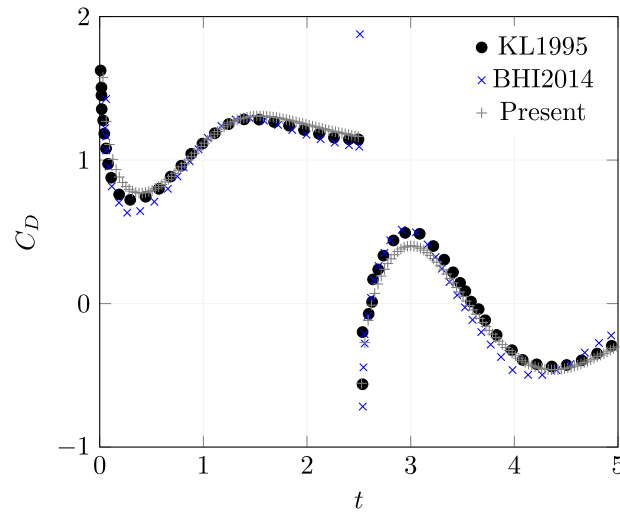


Fig. 17. Comparison of the evolution of the drag coefficient up to  $t = 5$  for the impulsively started and then stopped cylinder at  $Re = 550$  with data by Koumoutsakos and Leonard (KL1995) [69] and Bergmann et al. (BHI2014) [65].

masses after the Archimedes' law; in the rotational equation (57c) the cylinder inertia is denoted by  $J_B = \pi r^4 \rho_s$ ; finally  $\mathbf{F}_f$  and  $M_f$  are the fluid dynamics forces and torque defined in (56), respectively.

The background mesh is uniform and Cartesian with cells of size  $h = 5 \times 10^{-2}$ . The foreground mesh fits the cylinder shape with the characteristic lengths of the cell varying from  $1.4 \times 10^{-3}$  to  $5 \times 10^{-2}$ . The time step is  $\Delta t = \min(h)/20$ . Since we are interested in simulating the cylinder up to the lower boundary, there exists a time  $t_0$  after which the foreground mesh overcomes the physical boundaries of the cavity, as showed in Fig. 18. In order to manage the part of the foreground mesh exceeding the physical domain, we extend the computational domain as  $\tilde{\Omega} = (0, 2) \times (-1, 2)$  such that the foreground mesh is always fully contained. Thus, the exceeding region is discretized by a part of the background and, and for any time  $t > t_0$ , by a part of the foreground mesh. In the whole computational domain a fluid-solid single flow is considered by modeling a solid material in the extended part (i.e., for any  $y < 0$ ). This single flow is computed via a penalization method [5]. With this approach the entire system is considered as a porous medium with a variable discontinuous permeability  $K$ . In particular, the extended domain simulates an impermeable body with a very low permeability (i.e.,  $K \ll 1$ ). In this case, the considered equation in place of (2) reads

$$\frac{\partial \mathbf{u}}{\partial t} + \nabla \cdot (\mathbf{u}\mathbf{u}^T) = -\nabla p + \frac{1}{Re} \Delta \mathbf{u} + \frac{\chi_W}{K} (\mathbf{u}_W - \mathbf{u}), \tag{58}$$

where  $\mathbf{u}_W$  is the velocity of the wall, zero in our case, and  $\chi_W$  is the characteristic function defined as

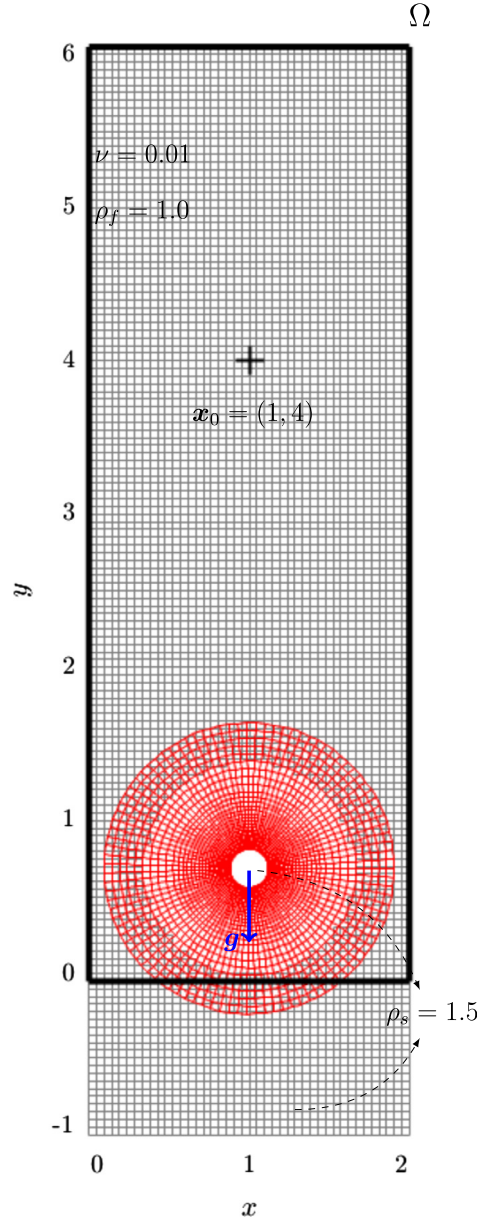


Fig. 18. Chimera configuration for the sedimentation cylinder.

$$\chi_W = \begin{cases} 1, & \text{in the wall} \\ 0, & \text{elsewhere} \end{cases} \tag{59}$$

In the limit of  $K \rightarrow 0$ , equation (58) tends to the Navier-Stokes equation (2) [5]. In this test case  $K = 10^{-8}$ . Despite in principle the penalization method can be used also for the cylinder, we remark that in this case we use is only for managing the extended part of the computational domain. In particular, we consider the solid below the wall having the same density of the cylinder (i.e.,  $\rho_s = 1.5$ ). Since the new reaction term in (58) affects the velocity, with respect to the fractional Chorin-Temam method, it is included in the predictor solution (7). Thus, it implies the ADER scheme to consider a reaction no-stiff source term [52]. In particular, in the local space-time Galerkin solution for equation (20), a pseudo-mass term arises as

$$\frac{\Delta t}{K} \langle \theta_m, \chi_W|_{\hat{\xi}_l} \theta_l \rangle \hat{q}_{k,l} \tag{60}$$

for  $m, l = 1, \dots, 27$ , with  $\chi_W|_{\hat{\xi}_l} = \chi_W(x(\hat{\xi}_l), y(\hat{\xi}_l))$  is the characteristic function composed with the spatial components of the reference map  $\mathcal{M}_i$  along the  $l$ -th tensor Gauss-Legendre quadrature point. Successively, for the fixed-point problem

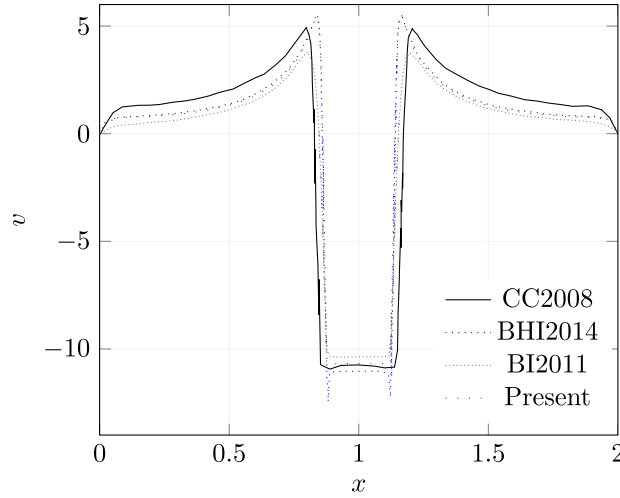


Fig. 19. Comparison of the vertical velocity  $v$  on a horizontal cut through the center of the cylinder at time  $t = 0.1$  for the sedimentation test case with data by Coquerelle and Cottet (CC2008) [70], Bergmann et al. (BHI2014) [65] and Bergmann and Iollo (BI2011) [64].

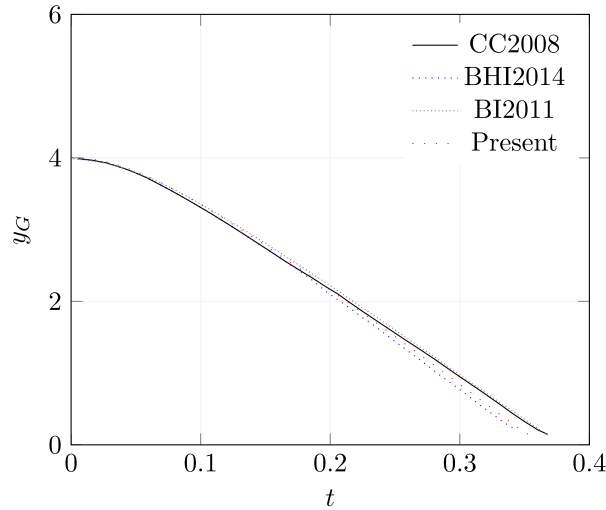


Fig. 20. Comparison of the evolution of the vertical position  $y_G$  of the center of the cylinder for the sedimentation test case with data by Coquerelle and Cottet (CC2008) [70], Bergmann et al. (BHI2014) [65] and Bergmann and Iollo (BI2011) [64].

(21), at the iteration  $r$ , this reaction term (60) yields an unknown component as  $\Delta t/K \langle \theta_m, \chi_W |_{\hat{\xi}_l} \theta_l \rangle \hat{q}_{k,l}^{r+1}$ . During the ADER correction step (27), the penalization term is just added at the left hand side of the space-time divergence form as

$$\nabla_{\mathbf{x},t} \cdot \mathbf{u}_k + \frac{\chi_W}{K} u_k = 0. \tag{61}$$

In order to write the FV scheme, by integrating the above expression in the physical space-time slab  $C_i^n$ , the method becomes

$$-|\Omega_i^n| \bar{u}_{k,i}^{*,n} + |\Omega_i^{n+1}| \bar{u}_{k,i}^{*,n+1} + \sum_{j=1}^4 \iint_{\Gamma_{ij}^n} \mathbf{u}_k \cdot \mathbf{n}_{\mathbf{x},t} \, d\Gamma + \iiint_{C_i^n} \frac{\chi_W}{K} u_k \, dC = 0. \tag{62}$$

Scheme (62) is not affected in the space-time fluxes by the new reaction term. For this reason, the procedure of the method remains the same as explained in Section 4.1. The simulation is stopped when the lowest point of the cylinder approaches the physical wall of the channel.

Figs. 19 and 20 show the validation for the vertical velocity on the horizontal line cutting the cylinder along the center and the evolution of the height of the cylinder, respectively. Present data present good agreement with all the ones from the literature. In particular it is possible to remark a closer match with the curves by Bergmann et al. [65]; indeed both

the present method and the method used in that paper are second-order accurate, while both references [64,70] present first-order accurate methods. Also in this case it is possible to remark the sensible decreasing of degrees of freedom needed by the numerical solution through the presented method with respect to the ones from the literature. In fact if the overset grid is composed of 9267 cells (i.e., 5964 in the background and 3663 in the foreground), grids employed in [70], [65] and [64] use about  $3 \times 10^6$ ,  $8 \times 10^5$  and  $2 \times 10^6$  cells.

## 7. Conclusions

We presented a FV scheme that is second-order accurate in space and time for the solution of the incompressible Navier-Stokes equations with moving meshes. The method is based on the Chorin-Temam fractional step method. The predictor velocity is solved through an extension of the ADER method for a nonlinear convective-diffusive system on a Chimera mesh with a compact data transmission condition for fringe cells, i.e., those cells devoted to the communication between the different meshes of the overset grid. The projection step exploits a FV hybrid method for the reconstruction of the pressure gradient. In particular a geometric approach is used for internal cells and a weighted expansion is employed for expressing the gradient along the fringe cells. We proved that the approaches for internal and fringe cells are the same in the limit of a no-shift overlapping condition. This result is achieved by properly minimizing a convex function for the local coefficients allowing to take into account both the second-order truncation of the solution and the distribution of data in the local stencil.

Overall, on the one hand, we solve for the first time the incompressible Navier-Stokes equations with an ADER-type scheme. On the other hand, since this method allows to treat spatial and temporal variables indistinctly, we discretize the evolutionary computational domain with chimera grids. This makes it possible to consider deformations that do not force the mesh to change topology [71].

The numerical results showed that the movement of the mesh does not introduce spurious oscillation to the numerical solution of the problem and that second-order accuracy is preserved in both space and time. In order to test the method, a wide range of canonical cases is exposed. Their validation confirms that the obtained data match the ones from the literature. In particular, results for tests where the exact solution is not available are always closer to the ones obtained by second-order methods. Moreover, at equal accuracy, the total number of cells for the overset grid (namely the degrees of freedom) is reduced by up to two orders of magnitude compared to the ones from the cited literature, where interface methods are used by employing a uniform Cartesian one-block mesh, similar to the background mesh used in this paper. With the sedimentation test case, we introduced a reaction term which is not present *a priori* in the original equation. In particular, we mixed the adapted ADER method for Chimera meshes with a penalization method in order not to cut part of the foreground mesh that overcomes the physical boundaries of the domain. This application highlights the versatility of the proposed method even in proximity of boundaries defined on other mesh blocks. Extension to three-dimensional flows on octree meshes is now envisaged.

## CRedit authorship contribution statement

**Michel Bergmann:** Conceptualization, Formal analysis, Investigation, Methodology, Supervision, Writing – review & editing. **Michele Giuliano Carlino:** Conceptualization, Formal analysis, Investigation, Methodology, Software, Validation, Visualization, Writing – original draft, Writing – review & editing. **Angelo Iollo:** Conceptualization, Formal analysis, Funding acquisition, Investigation, Methodology, Project administration, Supervision, Writing – review & editing. **Haysam Telib:** Conceptualization, Investigation, Methodology, Supervision, Writing – review & editing.

## Declaration of competing interest

The authors declare that they have no known competing financial interests or personal relationships that could have appeared to influence the work reported in this paper.

## Acknowledgements

The authors acknowledge the support by European Union's Horizon 2020 research and innovation programme under the Marie Skłodowska-Curie Actions, grant agreement 872442 (ARIA). MGC is pleased to thank the company Optimad Engineering srl for hosting him during part of the research in Turin. Numerical simulations presented in this paper were carried out using the PlaFRIM experimental testbed, supported by INRIA, CNRS (LABRI and IMB), Université de Bordeaux, Bordeaux INP and Conseil Régional d'Aquitaine (<https://www.plafrim.fr/>).

## References

- [1] C.W. Hirt, A.A. Amsden, J. Cook, An arbitrary Lagrangian-Eulerian computing method for all flow speeds, *J. Comput. Phys.* 14 (3) (1974) 227–253.
- [2] F. Duarte, R. Gormaz, S. Natesan, Arbitrary Lagrangian-Eulerian method for Navier-Stokes equations with moving boundaries, *Comput. Methods Appl. Mech. Eng.* 193 (45–47) (2004) 4819–4836.

- [3] F. Gibou, R.P. Fedkiw, L.-T. Cheng, M. Kang, A second-order-accurate symmetric discretization of the Poisson equation on irregular domains, *J. Comput. Phys.* 176 (1) (2002) 205–227.
- [4] R. Mittal, G. Iaccarino, Immersed boundary methods, *Annu. Rev. Fluid Mech.* 37 (2005) 239–261.
- [5] P. Angot, C.-H. Bruneau, P. Fabrie, A penalization method to take into account obstacles in incompressible viscous flows, *Numer. Math.* 81 (4) (1999) 497–520.
- [6] R. Glowinski, T.-W. Pan, J. Periaux, A fictitious domain method for Dirichlet problem and applications, *Comput. Methods Appl. Mech. Eng.* 111 (3–4) (1994) 283–303.
- [7] C.S. Peskin, The immersed boundary method, *Acta Numer.* 11 (2002) 479–517.
- [8] R. Abgrall, H. Beaugendre, C. Dobrzynski, An immersed boundary method using unstructured anisotropic mesh adaptation combined with level-sets and penalization techniques, *J. Comput. Phys.* 257 (2014) 83–101.
- [9] E. Volkov, The method of composite meshes for finite and infinite regions, *Autom. Programming, Numer. Methods Funct. Analysis* 96 (96) (1970) 145.
- [10] J. Benek, P. Buning, J. Steger, A 3-d Chimera grid embedding technique, in: 7th Computational Physics Conference, 1985, p. 1523.
- [11] R. Meakin, Chapter 11: composite overset structured grids, in: J.F. Thompson, B.K. Soni, N.P. Weatherill (Eds.), *Handbook of Grid Generation*, CRC, 1999.
- [12] N.A. Petersson, Hole-cutting for three-dimensional overlapping grids, *SIAM J. Sci. Comput.* 21 (2) (1999) 646–665.
- [13] G. Starius, Constructing orthogonal curvilinear meshes by solving initial value problems, *Numer. Math.* 28 (1) (1977) 25–48.
- [14] G. Starius, On composite mesh difference methods for hyperbolic differential equations, *Numer. Math.* 35 (3) (1980) 241–255.
- [15] G. Starius, Composite mesh difference methods for elliptic boundary value problems, *Numer. Math.* 28 (2) (1977) 243–258.
- [16] J.W. Banks, W.D. Henshaw, A.K. Kapila, D.W. Schwendeman, An added-mass partition algorithm for fluid–structure interactions of compressible fluids and nonlinear solids, *J. Comput. Phys.* 305 (2016) 1037–1064.
- [17] J.W. Banks, W.D. Henshaw, B. Sjögreen, A stable FSI algorithm for light rigid bodies in compressible flow, *J. Comput. Phys.* 245 (2013) 399–430.
- [18] D. Schwendeman, A. Kapila, W. Henshaw, A study of detonation diffraction and failure for a model of compressible two-phase reactive flow, *Combust. Theory Model.* 14 (3) (2010) 331–366.
- [19] J.W. Banks, D.W. Schwendeman, A.K. Kapila, W.D. Henshaw, A high-resolution Godunov method for compressible multi-material flow on overlapping grids, *J. Comput. Phys.* 223 (1) (2007) 262–297.
- [20] G. Chesshire, W.D. Henshaw, Composite overlapping meshes for the solution of partial differential equations, *J. Comput. Phys.* 90 (1) (1990) 1–64.
- [21] W.D. Henshaw, *Cgins reference manual: an overture solver for the incompressible Navier-Stokes equations on composite overlapping grids*, in: Centre for Applied Scientific Computing, 2012.
- [22] I.-T. Chiu, R. Meakin, On automating domain connectivity for overset grids, in: 33rd Aerospace Sciences Meeting and Exhibit, 1995, p. 854.
- [23] J. Guerrero, *Overset composite grids for the simulation of complex moving geometries*, DICAT, University of Genoa, Italy, 2006.
- [24] Z. Wang, A fully conservative interface algorithm for overlapped grids, *J. Comput. Phys.* 122 (1) (1995) 96–106.
- [25] M.-S. Liou, Y. Zheng, A novel approach of three-dimensional hybrid grid methodology: Part 2. Flow solution, *Comput. Methods Appl. Mech. Eng.* 192 (37–38) (2003) 4173–4193.
- [26] W.D. Henshaw, On multigrid for overlapping grids, *SIAM J. Sci. Comput.* 26 (5) (2005) 1547–1572.
- [27] G. Houzeaux, J. Cajas, M. Discacciati, B. Eguzkitza, A. Gargallo-Peiró, M. Rivero, M. Vázquez, Domain decomposition methods for domain composition purpose: chimera, overset, gluing and sliding mesh methods, *Arch. Comput. Methods Eng.* 24 (4) (2017) 1033–1070.
- [28] K.-H. Kao, M.-S. Liou, Advance in overset grid schemes—from chimera to dragon grids, *AIAA J.* 33 (10) (1995) 1809–1815.
- [29] M. Bergmann, A. Fondanèche, A. Iollo, A fully eulerian finite volume method for the simulation of fluid–structure interactions on amr enabled quadtree grids, in: *International Conference on Finite Volumes for Complex Applications*, Springer, 2020, pp. 765–772.
- [30] A.J. Chorin, Numerical solution of the Navier-Stokes equations, *Math. Comput.* 22 (104) (1968) 745–762.
- [31] R. Temam, Sur l'approximation de la solution des équations de Navier-Stokes par la méthode des pas fractionnaires (ii), *Arch. Ration. Mech. Anal.* 33 (5) (1969) 377–385.
- [32] M. Dumbser, W. Boscheri, M. Semplice, G. Russo, Central weighted eno schemes for hyperbolic conservation laws on fixed and moving unstructured meshes, *SIAM J. Sci. Comput.* 39 (6) (2017) A2564–A2591.
- [33] V.A. Titarev, E.F. Toro, ADER schemes for three-dimensional non-linear hyperbolic systems, *J. Comput. Phys.* 204 (2) (2005) 715–736.
- [34] V.A. Titarev, E.F. Toro, ADER: arbitrary high order Godunov approach, *J. Sci. Comput.* 17 (1) (2002) 609–618.
- [35] C.E. Castro, E.F. Toro, Solvers for the high-order Riemann problem for hyperbolic balance laws, *J. Comput. Phys.* 227 (4) (2008) 2481–2513.
- [36] M. Bergmann, M.G. Carlino, A. Iollo, Second order ADER scheme for unsteady advection-diffusion on moving overset grids with a compact transmission condition, *SIAM J. Sci. Comput.* 44 (1) (2022) A524–A553.
- [37] E. Bertolazzi, G. Manzini, A cell-centered second-order accurate finite volume method for convection–diffusion problems on unstructured meshes, *Math. Models Methods Appl. Sci.* 14 (08) (2004) 1235–1260.
- [38] Y. Coudière, J.-P. Vila, P. Villedieu, Convergence rate of a finite volume scheme for a two dimensional convection-diffusion problem, *ESAIM: Math. Model. Numer. Analysis* 33 (3) (1999) 493–516.
- [39] A. Raeli, M. Bergmann, A. Iollo, A finite-difference method for the variable coefficient Poisson equation on hierarchical cartesian meshes, *J. Comput. Phys.* 355 (2018) 59–77.
- [40] M.J. Berger, J. Olinger, Adaptive mesh refinement for hyperbolic partial differential equations, *J. Comput. Phys.* 53 (3) (1984) 484–512.
- [41] M.M. Rai, A conservative treatment of zonal boundaries for Euler equation calculations, *J. Comput. Phys.* 62 (2) (1986) 472–503.
- [42] Y. Moon, M.-S. Liou, Conservative treatment of boundary interfaces for overlaid grids and multi-level grid adaptations, in: 9th Computational Fluid Dynamics Conference, 1989, p. 1980.
- [43] J.A. Wright, W. Shyy, A pressure-based composite grid method for the Navier-Stokes equations, *J. Comput. Phys.* 107 (2) (1993) 225–238.
- [44] E. Atta, Component-adaptive grid interfacing, in: 19th Aerospace Sciences Meeting, 1981, p. 382.
- [45] B. Kreiss, Construction of a curvilinear grid, *SIAM J. Sci. Stat. Comput.* 4 (2) (1983) 270–279.
- [46] J. Benek, J. Steger, F.C. Dougherty, A flexible grid embedding technique with application to the Euler equations, in: 6th Computational Fluid Dynamics Conference, Danvers, 1983, p. 1944.
- [47] F. Meng, J. Banks, W. Henshaw, D. Schwendeman, Fourth-order accurate fractional-step imex schemes for the incompressible Navier–Stokes equations on moving overlapping grids, *Comput. Methods Appl. Mech. Eng.* 366 (2020) 113040.
- [48] K. Mittal, S. Dutta, P. Fischer, Nonconforming Schwarz-spectral element methods for incompressible flow, *Comput. Fluids* 191 (2019) 104237.
- [49] A. Sharma, S. Ananthan, J. Sitaraman, S. Thomas, M.A. Sprague, Overset meshes for incompressible flows: on preserving accuracy of underlying discretizations, *J. Comput. Phys.* 428 (2021) 109987.
- [50] B. Roget, J. Sitaraman, Robust and efficient overset grid assembly for partitioned unstructured meshes, *J. Comput. Phys.* 260 (2014) 1–24.
- [51] R. Mittal, H. Dong, M. Bozkurttas, F. Najjar, A. Vargas, A. Von Loebbecke, A versatile sharp interface immersed boundary method for incompressible flows with complex boundaries, *J. Comput. Phys.* 227 (10) (2008) 4825–4852.
- [52] A. Hidalgo, M. Dumbser, ADER schemes for nonlinear systems of stiff advection–diffusion–reaction equations, *J. Sci. Comput.* 48 (1) (2011) 173–189.
- [53] W. Boscheri, M. Dumbser, Arbitrary-Lagrangian-Eulerian one-step WENO finite volume schemes on unstructured triangular meshes, *Commun. Comput. Phys.* 14 (5) (2013) 1174–1206.

- [54] G.B. Nagy, O.E. Ortiz, O.A. Reula, The behavior of hyperbolic heat equations' solutions near their parabolic limits, *J. Math. Phys.* 35 (8) (1994) 4334–4356.
- [55] E.F. Toro, G.I. Montecinos, Advection-diffusion-reaction equations: hyperbolization and high-order ADER discretizations, *SIAM J. Sci. Comput.* 36 (5) (2014) A2423–A2457.
- [56] C.-H. Bruneau, M. Saad, The 2d lid-driven cavity problem revisited, *Comput. Fluids* 35 (3) (2006) 326–348.
- [57] T. Kawamura, H. Takami, K. Kuwahara, New higher-order upwind scheme for incompressible Navier-Stokes equations, in: *Ninth International Conference on Numerical Methods in Fluid Dynamics*, Springer, 1985, pp. 291–295.
- [58] B. Leonard, The ultimate conservative difference scheme applied to unsteady one-dimensional advection, *Comput. Methods Appl. Mech. Eng.* 88 (1) (1991) 17–74.
- [59] U. Ghia, K.N. Ghia, C. Shin, High-re solutions for incompressible flow using the Navier-Stokes equations and a multigrid method, *J. Comput. Phys.* 48 (3) (1982) 387–411.
- [60] A. Vreman, A staggered overset grid method for resolved simulation of incompressible flow around moving spheres, *J. Comput. Phys.* 333 (2017) 269–296.
- [61] G. Jin, M. Braza, A nonreflecting outlet boundary condition for incompressible unsteady Navier-Stokes calculations, *J. Comput. Phys.* 107 (2) (1993) 239–253.
- [62] P. Ploumhans, G. Winckelmans, Vortex methods for high-resolution simulations of viscous flow past bluff bodies of general geometry, *J. Comput. Phys.* 165 (2) (2000) 354–406.
- [63] M. Bergmann, *Optimisation aérodynamique par réduction de modele pod et contrôle optimal, application au sillage laminaire d'un cylindre circulaire*, Institut National Polytechnique de Lorraine, 2004.
- [64] M. Bergmann, A. Iollo, Modeling and simulation of fish-like swimming, *J. Comput. Phys.* 230 (2) (2011) 329–348.
- [65] M. Bergmann, J. Hovnanian, A. Iollo, An accurate cartesian method for incompressible flows with moving boundaries, *Commun. Comput. Phys.* 15 (5) (2014) 1266–1290.
- [66] M. Braza, P. Chassaing, H.H. Minh, Numerical study and physical analysis of the pressure and velocity fields in the near wake of a circular cylinder, *J. Fluid Mech.* 165 (1986) 79–130.
- [67] J.-W. He, R. Glowinski, R. Metcalfe, A. Nordlander, J. Periaux, Active control and drag optimization for flow past a circular cylinder: I. oscillatory cylinder rotation, *J. Comput. Phys.* 163 (1) (2000) 83–117.
- [68] R.D. Henderson, Details of the drag curve near the onset of vortex shedding, *Phys. Fluids* 7 (9) (1995) 2102–2104.
- [69] P. Koumoutsakos, A. Leonard, High-resolution simulations of the flow around an impulsively started cylinder using vortex methods, *J. Fluid Mech.* 296 (1995) 1–38.
- [70] M. Coquerelle, G.-H. Cottet, A vortex level set method for the two-way coupling of an incompressible fluid with colliding rigid bodies, *J. Comput. Phys.* 227 (21) (2008) 9121–9137.
- [71] S. Busto, S. Chiocchetti, M. Dumbser, E. Gaburro, I. Peshkov, High order ADER schemes for continuum mechanics, *Front. Phys.* 8 (2020) 32.